

## Article

# Mineralogy, Geochemistry and Fluid Inclusion Study of the Stibnite Vein-Type Mineralization at Rizana, Northern Greece

Christos L. Stergiou <sup>1</sup>, Grigorios-Aarne Sakellaris <sup>1</sup>, Vasilios Melfos <sup>1,\*</sup>, Panagiotis Voudouris <sup>2</sup>,  
Lambrini Papadopoulou <sup>1</sup>, Nikolaos Kantiranis <sup>1</sup> and Evaggelos Skoupras <sup>1</sup>

<sup>1</sup> Faculty of Geology, Aristotle University of Thessaloniki, 54124 Thessaloniki, Greece

<sup>2</sup> Faculty of Geology and Geoenvironment, National and Kapodistrian University of Athens, 15784 Athens, Greece

\* Correspondence: melfosv@geo.auth.gr

**Abstract:** The stibnite mineralization at Rizana (Kilkis ore district; Serbo-Macedonian metallogenic province; northern Greece) occurs along a NE–SW-trending brittle shear-zone, which transects a two-mica and an augen-gneiss of the Vertiskos Unit. Barren Triassic A-type granites and satellite pegmatites and aplites, as well as Oligocene-Miocene plutonic, subvolcanic and volcanic rocks that are variably hydrothermally altered and mineralized, outcrop in the broader region. The mineralization appears as veins, discordant lodes and disseminations. Veins and discordant lodes exhibit massive and brecciated textures. Historic underground mining (1930s–1950s) produced 9000 t of stibnite ore, grading 40% Sb on average. The main ore mineral assemblage includes stibnite + berthierite + sphalerite + pyrite + chalcopyrite + native antimony and traces of wolframite, galena, tetrahedrite, marcasite, pyrrhotite, arsenopyrite, realgar, native arsenic and native gold. Quartz, minor barite and ankerite are the gangue minerals. Sericitization and silicification developed along the shear-zone, forming hydrothermal halos of moderate intensity in the two-mica gneiss. Locally, valentinite, goethite and claudetite are present due to the supergene oxidation of the stibnite mineralization. Bulk ore geochemistry shows enrichments in specific elements including As, Au, Cd, Se, Tl and W. Fluid inclusion microthermometry showed that the mineralization was formed under a limited range of temperatures and salinities. The fluids had low to slightly moderate salinities (6.6–8.1 wt% equiv. NaCl) with low homogenization temperatures (217–254 °C, with a maximum at 220 °C).

**Keywords:** antimony; stibnite; vein mineralization; Rizana; Vertiskos Unit; Serbo-Macedonian Massif; Greece; fluid inclusions



**Citation:** Stergiou, C.L.; Sakellaris, G.-A.; Melfos, V.; Voudouris, P.; Papadopoulou, L.; Kantiranis, N.; Skoupras, E. Mineralogy, Geochemistry and Fluid Inclusion Study of the Stibnite Vein-Type Mineralization at Rizana, Northern Greece. *Geosciences* **2023**, *13*, 61. <https://doi.org/10.3390/geosciences13020061>

Academic Editors: Jesus Martinez-Frias, Domenico Montanari and Evgeniy V. Kislov

Received: 28 December 2022

Revised: 15 February 2023

Accepted: 15 February 2023

Published: 17 February 2023



**Copyright:** © 2023 by the authors. Licensee MDPI, Basel, Switzerland. This article is an open access article distributed under the terms and conditions of the Creative Commons Attribution (CC BY) license (<https://creativecommons.org/licenses/by/4.0/>).

## 1. Introduction

Antimony (Sb) is a lustrous, brittle and gray-colored metalloid that has a long history of use in human societies [1]. It has been known since 4000 BCE and was first used in eyebrown paints and later in metallurgy and in copper coatings [1]. During the 20th century, Sb was extensively sourced and used in lead metallurgy, for the production of ammunition and in the production of lead–acid batteries [1]. In the 21st century, Sb (as Sb<sub>2</sub>O<sub>3</sub>) is considered as a prominent critical raw material with applications related to flame retardants and aerospace–defense (e.g., optical and communication instruments, laser sighting) industries [2]. Antimony is a chalcophile element, rarely found in native form, and is mainly bound with sulfur to form stibnite (Sb<sub>2</sub>S<sub>3</sub>). In addition, antimony affiliated with copper, lead and silver forms a series of more than 100 minerals, including sulfosalts, such as tetrahedrite and famatinite [1,2].

In terms of ore geology, antimony is a principal commodity in various styles of ore deposits, for example, orogenic, Carlin-type and in veins (cf. five element veins after [3]) related to arsenide systems formed under continental rifting [3]. Additionally, antimony and stibnite can be found in deposits formed in volcanogenic seafloor settings, as well

as in epithermal vein-type mineralization and in sediment-hosted distal-disseminated mineralization located in the periphery of porphyry systems [3–8]. Stibnite hosted in epithermal quartz veins ( $T = 50$  to  $200\text{ }^{\circ}\text{C}$ ) is the primary Sb ore [1,5]. More than 50% of the world Sb production and reserves come from the Xiangzhong metallogenic province in China, where stibnite is found in structurally controlled vein-style mineralization hosted in sedimentary or metamorphic rocks distal to intrusions [9,10].

Although stibnite is ubiquitous in the Sb vein-type mineralization, a variety of minerals, such as low temperature sulfides, sulfosalts and arsenides, may also be incorporated [11,12]. Antimony is geochemically related to Hg and As and substitutes for Bi, Pb, As and S [2]. Thus, substitutions and micron- to nano-scale mineral inclusions in stibnite reflect variations in ore geochemistry related to Cu, Pb and As, as well as Au, Ag, Bi, Hg, In, Tl, Mo, Sn, Co, Cr, V, Zn, Ni, Ga, Ge, Rb, Sr, Pd and Cd enrichment [2,9]. In some other cases, the evolution from mesothermal to epithermal conditions may result in more complex mineralogy, as is the case with wolframite-scheelite bearing Sb vein-type deposits of Thailand [5].

The Serbo-Macedonian metallogenic belt (SMMB) spans from Serbia to northern Greece and is considered a Pb–Zn–Ag dominant district, including also a significant Au endowment [13]. Additionally, several polymetallic deposits and prospects incorporate antimony enrichments. Such examples include the Allchar Au–As–Sb–Tl deposit and the Lojane As–Sb deposit in North Macedonia, the Rujevac Sb–Pb–Zn–As deposit in Serbia, as well as the Janjevo As–Sb–Tl–Pb  $\pm$  Hg  $\pm$  Au deposit in Kosovo [14–18].

In northern Greece, the SMMB includes the Kilkis ore district and part of the Chalkidiki ore district (Figure 1). Several deposits and prospects related to Cenozoic magmatic-hydrothermal activity, which are enriched in Cu, Au and critical metals (e.g., Ag, Bi, Co, Sb, Te, REE, PGM), are hosted in basement rocks belonging to the Vertiskos Unit [6,8,19–24] (Figure 1).

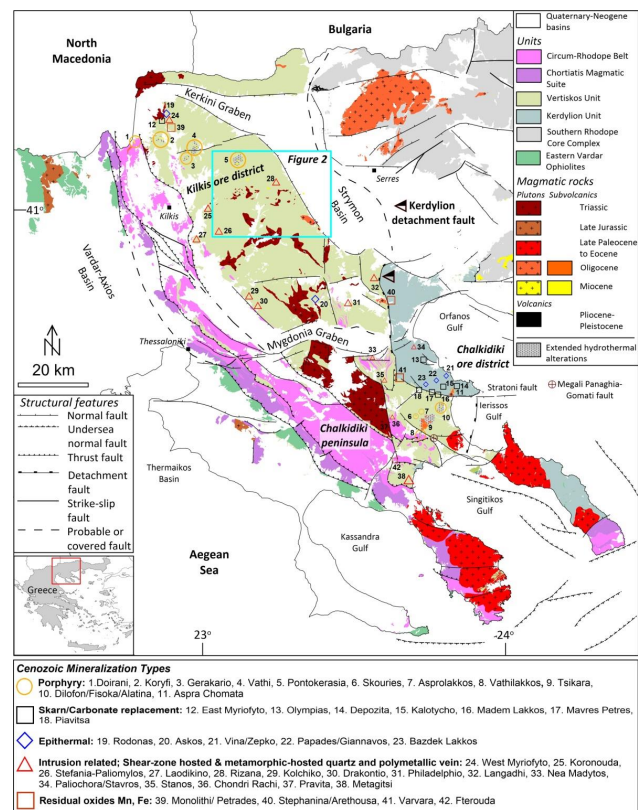


Figure 1. The geological setting of Cenozoic magmatism and related mineralization along the Vertiskos and Kerdylon Units (modified after [6,20,23,24]).

The Kilkis ore district includes porphyry, carbonate replacement, epithermal, intrusion related and residual oxides mineralization types associated with the Cenozoic magmatism of the Vertiskos Unit [6,19,23,24] (Figure 1). The regional mineral potential remains largely uninvestigated by modern exploration means [6,19,20,25–28].

The major Sb deposits and prospects in the region are located at Gerakario, Philadelphio and Rizana [8,28] (Figure 1). Furthermore, significant Sb-mineralization in Greece is found at Kallintiri (Thrace) and Chios island (Aegean Sea) [6,20,29]. At Gerakario, stibnite is hosted in epithermal veins found in the periphery of a porphyry Cu–Au deposit [8]. The metallic assemblage includes stibnite, berthierite, native antimony, pyrite, arsenopyrite, marcasite, pyrrhotite, chalcopyrite, löllingite and native gold [8]. The maximum content of critical metals measured in the Sb-ore includes: Sb (54.7 wt.%), Co (<1.8 ppm), Ag (<1.2 ppm), Ga (<0.16 ppm), Ce (<0.12 ppm), Au (<0.05 ppm), Cd (<0.05 ppm), La (<0.04 ppm) and Bi (<0.03 ppm) [8]. Exploration workings in the area held between the 1970s and the 1990s were targeted on Cu, Au and Mo. The Sb-mineralization was mined during the 1930s, with the extracted amount of ore remaining unknown, while estimations on Sb resources or reserves are not available [8].

Massive and discordant veins hosted in a shear-zone accommodate the Sb-mineralization at Philadelphio [19] (Figure 1). Ore minerals include stibnite, arsenopyrite, chalcopyrite, chalcostibite, scheelite, kermesite, marcasite, pyrite, pyrrhotite, sphalerite, stibiconite, tetrahedrite, covellite, wolframite, zinkenite, melnikovite and native gold [30]. Indicated resources include 10.08 Mt of ore, grading 3.36 wt.% of Sb [30].

At Rizana (also mentioned as Lachanas; Figure 1) the Sb deposit is hosted in a silicified brittle shear-zone crosscutting the basement metamorphic rocks. Locally, it is enriched in W found as wolframite. Previous publications have explored the genesis, the mineral association and the potential ore application [31–35]. In this study, we present new data on mineralogy and geochemistry of the host two-mica gneiss and of the ore mineralization at Rizana, and we share formula calculations on stibnite, pyrite, sphalerite, chalcopyrite, berthierite and valentinite. In addition, we investigate the distribution of the critical metals in the mineralization after bulk geochemistry. Finally, based on microthermometric data collected from the fluid inclusions in quartz from the stibnite mineralization, we highlight the ore forming history and fluid evolution at Rizana. The results advance the exploration potential by sharing new ore geochemical data and by clarifying the genetic model of the Sb deposit.

## 2. Geological Setting

### 2.1. Regional Geology

The Vertiskos Unit (i.e., the Serbo-Macedonian Massif in northern Greece) is a poly-tectonic and poly-metamorphosed geotectonic and basement zone, which along with Triassic plutonic rocks (within plate; A-type granites) constitutes a Gondwana-derived distinct basement unit accreted to the Hellenic orogen during Late Jurassic–Early Cretaceous [36–39] (Figures 1 and 2). The Eocene–Oligocene Kerdylion detachment fault separates the Vertiskos Unit and the Circum–Rhodope belt from the Kerdylion Unit and the Southern Rhodope Core Complex to the east [38]. The Kerdylion detachment and the Miocene Strymon detachment faults are related to the extensional collapse of the Vertiskos Unit towards SSW between Late Cretaceous and Miocene [38]. The formation of the Cenozoic mineralization at Vertiskos was set under this extensional regime and was controlled by ENE–WSW and eastward-trending shears [40]. Numerous E–W, NW–SE and NE–SW trending normal to oblique faults and N–S trending strike-slip faults further describe the regional framework [40].

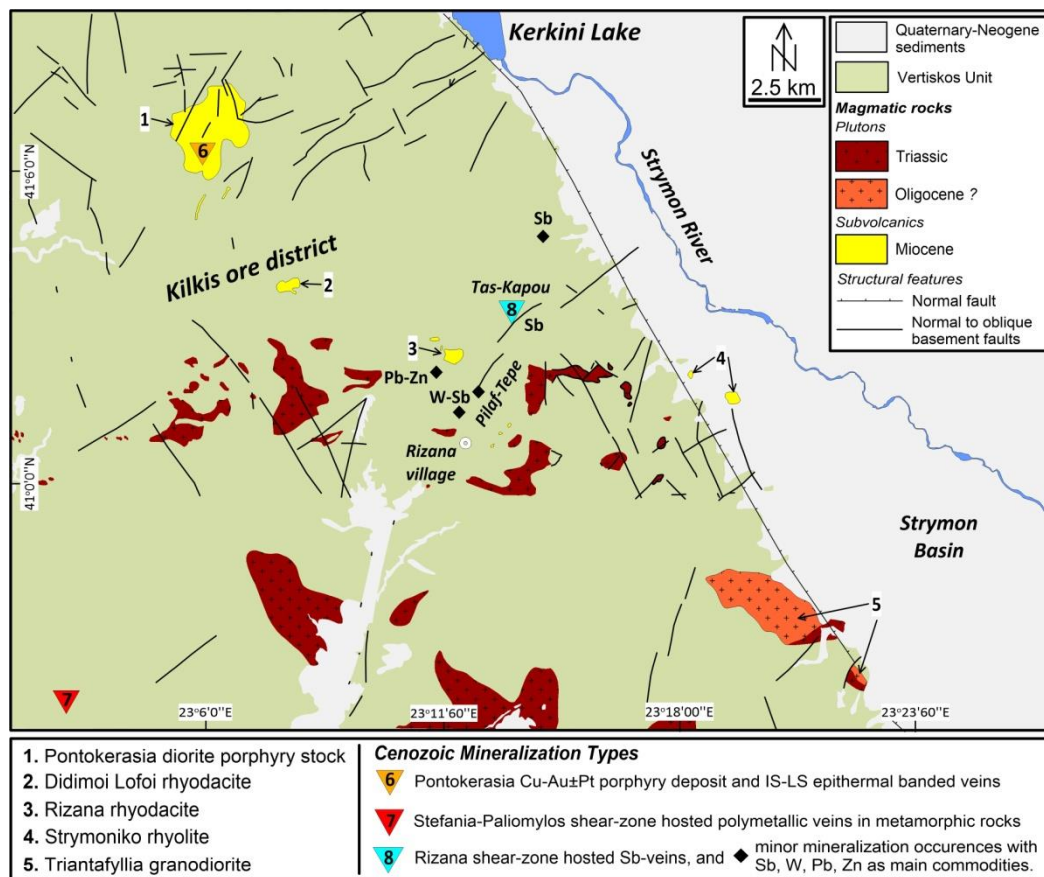


**Figure 2.** Geological map of the Rizana region (for the location of the map see Figure 1, modified after [23,24,35,41–43]).

In the broader Rizana area, metamorphic rocks belonging to the Vertiskos Unit include mainly two-mica gneiss, as well as augen- and muscovite-gneiss of Silurian age. In these rocks, Mesozoic amphibolites and serpentized peridotites are found intercalated [36] (Figure 2). The dominant metamorphic overprint on the basement rocks is associated with late-Jurassic to early Cretaceous upper amphibolite facies metamorphism [39]. A distinct group of pegmatites and aplitic sills ( $300 \pm 10$  Ma; K/Ar muscovite ages after [44]) are found mainly concordant to the local schistosity and include zoned tourmaline [45].

The Triassic A-type granites (mean age:  $228.3 \pm 5.6$  Ma; U/Pb zircon age after [37]) are voluminous, locally schistosed and barren [46,47]. Numerous pegmatites and aplites related to the Triassic magmatism are found both crosscutting and parallel to the local schistosity.

Several Cenozoic (Oligocene? to Miocene) magmatic rocks outcrop in the area [41–43,48] (Figure 2). They include silica-saturated, calc-alkaline to slightly alkaline plutonic to subvolcanic rocks, which locally exhibit porphyritic textures [42,48]. The most significant is the Pontokerasia diorite porphyry stock that is associated with a Cu–Au±Pt porphyry occurrence and low- to intermediate-sulfidation epithermal banded veins [6,41]. Minor magmatic rocks include the rhyodacites of Didimoi Lofoi and Rizana, which are hydrothermally altered (sericitic alteration) and contain pyrite disseminations, and the barren Strymoniko rhyolite and Triantafyllia granodiorite [42] (Figure 2). The Rizana rhyodacite consists of quartz, plagioclase, biotite, traces of amphibole, while accessory minerals include apatite, ilmenite, zircon and rutile. The alteration assemblage contains quartz, sericite and calcite [42].

Cenozoic structures include the large fault zone separating Vertiskos Unit from the Quaternary-Neogene sediments of the Strymon basin, and minor NE–SW and NW–SE trending normal to oblique faults, which transect the local ductile deformation fabrics [40] (Figure 2). The NE–SW set of faults is related to the development of a mineralized

shear-zone transecting the two-mica gneiss and the augen-gneiss of the Vertiskos Unit (Figure 3a,b).

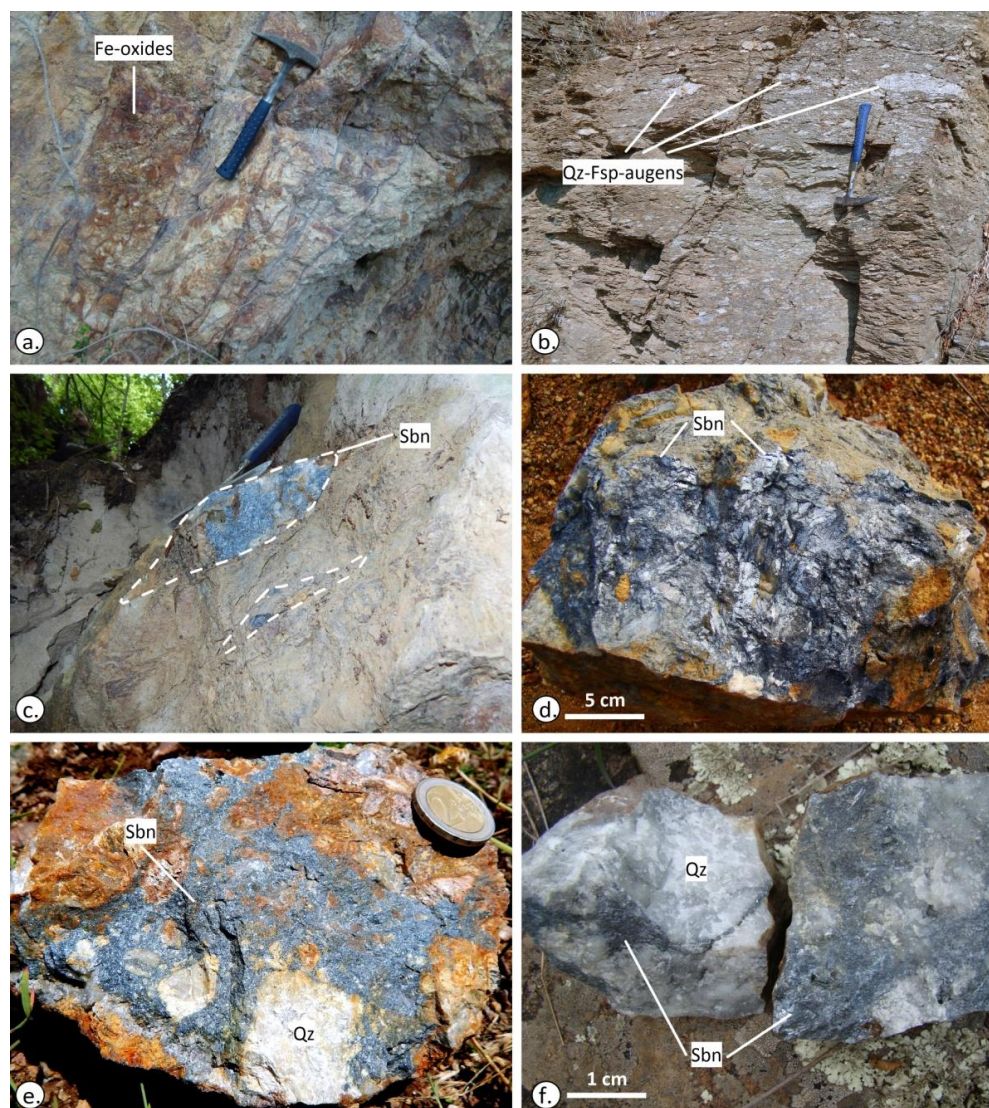


**Figure 3.** Field photographs of the local lithology and the stibnite mineralization: (a) Fe-oxides in the two-mica gneiss; (b) Augen-gneiss outcrop with numerous quartz (Qtz)–feldspar (Fsp)–augens of various sizes along the foliation; (c) Dashed lines outline two discordant lodes of stibnite (Sbn) mineralization; (d) Massive and granular stibnite (Sbn) mineralization; (e) Massive (Sbn) cements brecciated quartz; (f) Fragments of a quartz–stibnite vein where stibnite (Sbn) fills spaces along quartz clusters (Photo courtesy: Vasilios Melfos).

## 2.2. The Sb Deposit at Rizana

The main stibnite mineralization at Rizana ( $41^{\circ}3'6.0192''$  N,  $23^{\circ}13'47.7552''$  E) is located approximately 3.8 km NE of the Rizana village and 2 km NE of the Rizana rhyodacite in an area called “Tas-Kapou” [31,33] (Figure 2). Several other minor outcrops of magmatic rocks are found in the broader area (Figure 2). The stibnite mineralization is controlled by a shear-zone (in average <8 m in width) that strikes  $N45^{\circ}E$  and dips  $70^{\circ}$  to NE on average. The shear-zone is described by brittle deformation, angular quartz fragments cemented by stibnite and intense silicification, while ductile deformation textures are not observed.

Ore morphology includes veins and discordant lodes exhibiting massive, granular and brecciated textures, and disseminations in quartz (Figure 3c–f). The mineralization consists of stibnite, and includes minor berthierite, sphalerite, pyrite, chalcopyrite and

native antimony, as well as traces of arsenopyrite, wolframite, galena, marcasite, pyrrhotite, realgar, tetrahedrite, native arsenic and native gold ([32,33], this study).

Quartz, barite and ankerite are the main gangue minerals, while valentinite ( $\text{Sb}_2\text{O}_3$ ), goethite and claudetite ( $\text{As}_2\text{O}_3$ ) were formed due to subsequent supergene oxidation ([32,33], this study). Hydrothermal alteration related to the mineralizing stage includes sericitization and silicification. The alteration assemblage includes quartz, sericite and rutile which form restricted, yet moderate in intensity, hydrothermal halos affecting mainly the two-mica gneiss (this study).

The main wolframite mineralization at Rizana is located approximately 1 km SE of the Rizana rhyodacite at “Pilaf-Tepe” area (Figure 2), while wolframite is a minor constituent of the “Tas-Kapou” stibnite mineralization. The wolframite mineralization is structurally bound in a silicified fault zone [33]. Primary minerals include mainly Fe–wolframite (=ferberite:  $\text{FeWO}_4$ ) and stibnite, while supergene oxidation resulted in the formation of tungstite ( $\text{WO}_3 \cdot \text{H}_2\text{O}$ ), cervantite ( $\text{Sb}^{3+}\text{Sb}^{5+}\text{O}_4$ ) and stibiconite ( $\text{Sb}^{3+}\text{Sb}^{5+}_2\text{O}_6(\text{OH})$ ) [32,33]. Minor base metal (Pb, Zn) veins are found at the periphery of the W–Sb–mineralization and near the Rizana rhyodacite (Figure 2).

Historic mining (1930–1950), including underground galleries set in three production levels, exploited 9000 t of stibnite ore, with up to 40% of Sb in the final concentrate [31] (Figure 4a,b). Underground mining was also targeted to wolframite (1910–1940), but the extracted amount of ore is unknown [31]. Beneficiation of the extracted stibnite ore was held by mechanic means outside the tunnels and by flotation near the neighboring Zevgolatio village before shipping [31] (Figure 4c,d). Indicated reserves from the historic mining report 50,000 to 100,000 t of stibnite ore and 1000 t of wolframite ore, while the measured reserves include 5000 t of stibnite ore with 0.3 wt.% of Sb in average [31].



**Figure 4.** Photographs from the sampling survey: (a) The entrance of an old gallery; (b) A gallery parallel to the stibnite mineralization. Vertical wall rocks indicate the area of the exploited stibnite mineralization; (c) Waste material deposited downhill and opposite to a gallery entrance. (d) The destroyed flotation infrastructure near Zevgolatio village in the 1990s (Photo courtesy: Vasilios Melfos).

### 3. Methods

#### 3.1. Field Work and Sampling

The study area was centered on the main Sb-mineralization at “Tas-Kapou” (Figure 5). Geological sampling was conducted along the surface by investigating the wall rocks along the entrances to the old galleries as well as the nearby scattered waste piles. Eleven samples were collected from the wall rocks (Figure 5; Table 1). Two samples (RZN01) are from the fresh two-mica gneiss; four samples (RZN02, RZN04, RZN06, RZN08) refer to hydrothermally altered and locally oxidized two-mica gneiss; one sample (RZN05) represents silicified two-mica gneiss bearing traces of stibnite mineralization; three samples (RZN03a, RZN03b, RZN07) are from the stibnite mineralization; and two samples (RZN09, RZN10) are from the quartz–stibnite veins (Table 1).

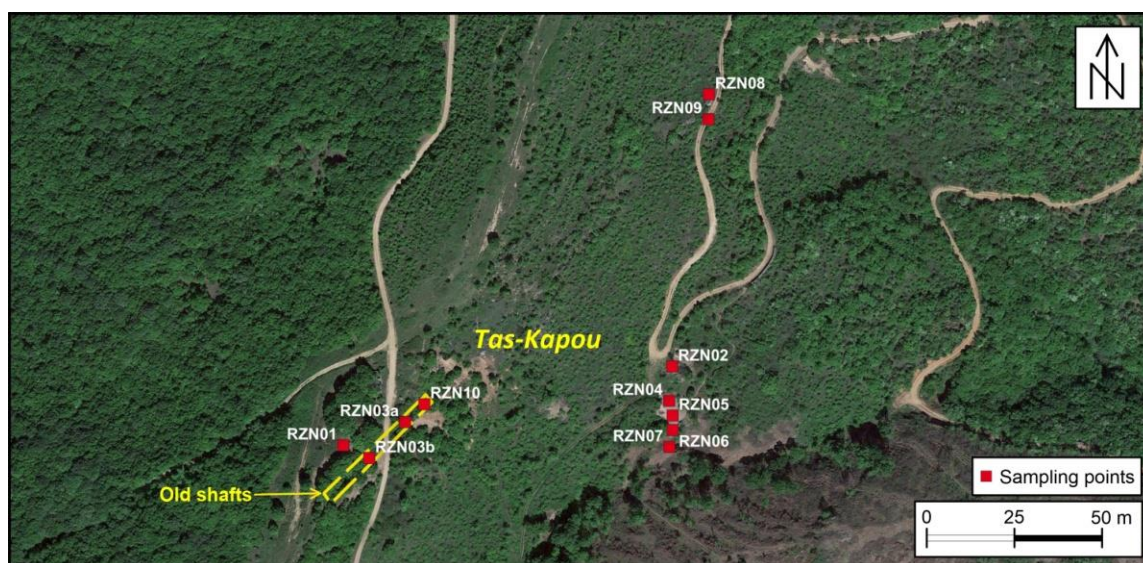


**Figure 5.** Satellite imagery of the sampling area at “Tas-Kapou”. The sampling points are shown, and the location of the main old galleries is highlighted in yellow.

**Table 1.** Sample identification numbers, localities (coordinates) and lithological descriptions.

Sample ID	Coordinates (Latitude/Longitude)	Lithological Description
RZN01	41.051658° 23.229640°	Two-mica gneiss; fresh
RZN02	41.052089° 23.232019°	Two-mica gneiss; sericitized and oxidized
RZN03a	41.051785° 23.230086°	Stibnite mineralization
RZN03b	41.051589° 23.229828°	Stibnite mineralization
RZN04	41.051901° 23.231996°	Two-mica gneiss; sericitized
RZN05	41.051821° 23.232021°	Two-mica gneiss; silicified with stibnite
RZN06	41.051742° 23.232022°	Two-mica gneiss; sericitized
RZN07	41.051649° 23.231998°	Stibnite mineralization
RZN08	41.053571° 23.232284°	Two-mica gneiss; sericitized and oxidized
RZN09	41.053435° 23.232280°	Quartz–stibnite vein
RZN10	41.051882° 23.230226°	Quartz–stibnite vein

#### 3.2. Optical Microscopy

Optical microscopy was conducted on 12 thin, polished and polished-thin sections produced from selected samples under a ZEISS Axioskop 40 dual reflected-transmitted light polarizing microscope at the Faculty of Geology, Aristotle University of Thessaloniki (AUTH).

### 3.3. Scanning Electron Microscopy

Scanning electron microscope (SEM) studies of mineralized samples were conducted at the Faculty of Sciences (AUTH), using a JEOL JSM-6390LV scanning electron microscope (SEM) equipped with an OXFORD INCA 300 energy dispersive system (EDS) (Oxford Instruments Ltd., Abingdon, UK). Set in the back-scattering electron (BSE) mode, the operating conditions were a 20 kV accelerating voltage and 0.4 mA probe current, 80 s analysis time, and a beam diameter of  $\approx 1 \mu\text{m}$ . Laboratory empirical corrections were performed to compensate for peak overlap. The  $\text{AgK}\alpha$ ,  $\text{AuK}\alpha$ ,  $\text{AsK}\alpha$ ,  $\text{BaK}\alpha$ ,  $\text{BiK}\alpha$ ,  $\text{CaK}\alpha$ ,  $\text{CdK}\alpha$ ,  $\text{CuK}\alpha$ ,  $\text{CoK}\alpha$ ,  $\text{FeK}\alpha$ ,  $\text{MgK}\alpha$ ,  $\text{MnK}\alpha$ ,  $\text{NiK}\alpha$ ,  $\text{SK}\alpha$ ,  $\text{SbK}\alpha$ ,  $\text{SeK}\alpha$ ,  $\text{SrK}\alpha$  and  $\text{ZnK}\alpha$  X-ray lines were used after the following standards: jadeite for Mg, wollastonite for Ca, pyrite for Fe and S, while synthetic compounds were used for Ag, Au, As, Ba, Bi, Cd, Cu, Co, Mn, Ni, Sb, Se, Sr and Zn. The SEM–EDS micro-analyses were targeted on mineral texture and chemistry of stibnite, pyrite, sphalerite, chalcopyrite, berthierite and valentinite (Supplementary Table S2).

### 3.4. Bulk Geochemical Analysis

A total of six mineralized (RZN03a, RZN03b, RZN07) and host rock (RZN04, RZN05, RZN08) samples were analyzed for major and trace elements. Pulps were digested in a 4-acid solution (hydrochloric, nitric, perchloric and hydrofluoric acids) and analyzed by means of multi-element inductively coupled plasma–mass spectrometry (ICP–MS) at MSALABS, Langley, Canada (Supplementary Table S1). Two bulk geochemical analyses of stibnite ore from the quartz–stibnite veins at Gerakario [8], and bulk geochemical analyses of the two-mica gneiss from the Vertiskos Unit [36], were considered for comparison in this study (Supplementary Table S1). Statistical graphs were plotted in Grapher software (Golden Software LLC).

### 3.5. Fluid Inclusion Microthermometry

Three doubly polished wafers of quartz from the stibnite mineralization (RZN03b) and the quartz–stibnite veins (RZN09, RZN10), were prepared at the University of Hamburg, Germany, and were studied for fluid inclusions. Microthermometric data were obtained using a LINKAM THM-600/TMS 90 heating–freezing stage coupled to a Leitz SM-LUX-POL microscope (Department of Mineralogy–Petrology–Economic Geology, AUTH). Organic reference substances with known melting points and ice ( $\text{H}_2\text{O}$ ) were used to calibrate the stage. The precision of the measurements was  $0.1 \text{ }^\circ\text{C}$  for temperatures between  $-180 \text{ }^\circ\text{C}$  and  $+200 \text{ }^\circ\text{C}$  and  $1 \text{ }^\circ\text{C}$  for temperatures above  $+200 \text{ }^\circ\text{C}$ . Calculation of the fluid compositions and properties were obtained using the software packages FLUIDS [49] and SoWat [50], while densities were calculated from equations proposed by Driesner [51].

## 4. Results

### 4.1. Host Rock

The two-mica gneiss is a brownish colored rock with foliation planes showing deep bronze and lustrous colors (Figure 6a). Locally, hydrothermal alteration and oxidation resulted in discolorization and reddish staining related to Fe–oxides (Figure 6b,c). It is folded and exhibits a micro- to coarse-grained poikiloblastic and locally lepidoblastic texture. It contains plagioclase, quartz, muscovite, biotite, K-feldspar, while the accessory minerals include zoisite, clinozoisite, epidote, rutile, apatite and zircon (Figure 6d,e).

The alteration assemblage includes sericite, chlorite, quartz and calcite related to sericitization and silicification. Hydrothermal quartz veins with sericite are found parallel or crosscut the foliation (Figure 6c,f). Intense hydrothermal alteration resulted in quartz recrystallization, biotite chloritization and locally to the complete replacement of plagioclase and K-feldspar by sericite.

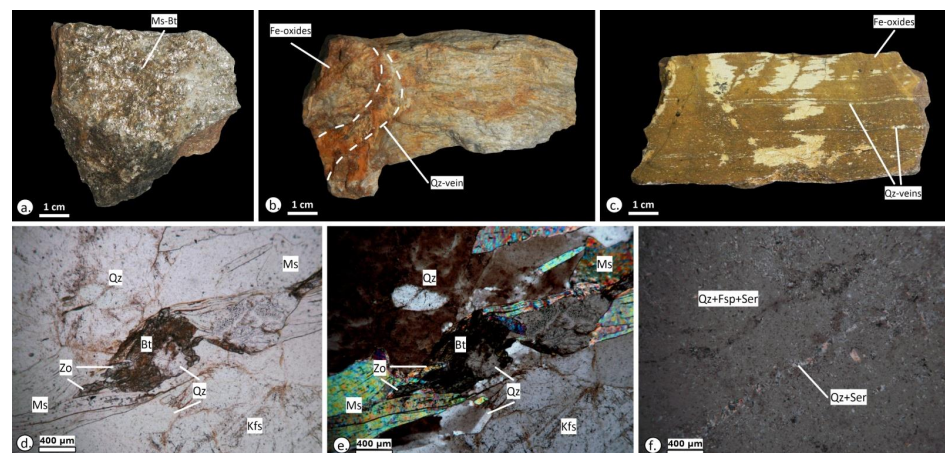


**Figure 6.** Hand specimens (a–c) and photomicrographs (plane polarized light: (b); cross-polarized light: (e,f)) of the two-mica gneiss from Rizana: (a) Lustrous muscovite (Ms) and biotite (Bt) parallel to schistosity; (b) A quartz (Qz) vein crosscutting a discolored and oxidized (Fe-oxides) two-mica gneiss; (c) extensively altered rock mass bearing wide Fe-oxides impregnations and hydrothermal quartz (Qz) veins developed along schistosity; (d,e) Muscovite (Ms) and biotite (Bt) intergrown with quartz (Qz) and K-feldspar (Kfs) and minor zoisite (Zo); (f) Quartz (Qz) and sericite (Ser) in a hydrothermal vein crosscutting a deformed ground mass containing quartz (Qz), feldspar (Fsp) and sericite (Ser).

#### 4.2. Ore Mineralogy at “Tas-Kapou”

Stibnite is the dominant ore mineral in “Tas Kapou” (Figures 7a–c and 8). Macroscopically, it has a lustrous lead-gray color and appears massive to granular (Figure 4d,e and Figure 7a–c), and locally as disseminated clusters or as radiating and elongated crystals in quartz (Figure 7d). Massive and granular textures are related to veins and discordant lodes where stibnite content may exceed 80% (Figures 4c and 7a–c). Stibnite disseminations fill up to 40% of the quartz–stibnite veins, where also radiating and elongate stibnite is found along cracks in quartz (Figure 7e).

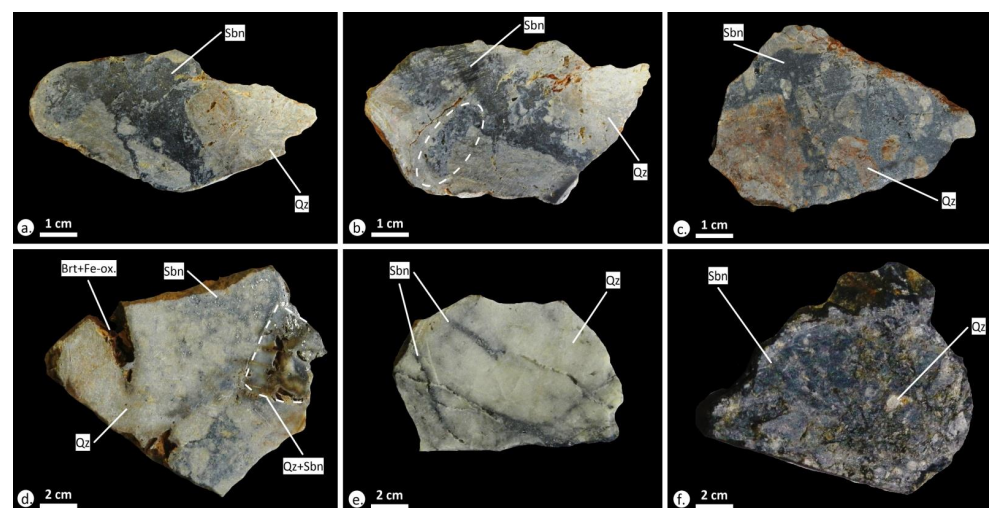


**Figure 7.** Hand specimens from the Sb ± W-mineralization at Rizana: (a) Massive stibnite (Sbn) cementing brecciated saccharoidal quartz (Qz); (b) Massive stibnite (Sbn) cementing locally micro-brecciated (dashed line) saccharoidal quartz (Qz); (c) Hydrothermal breccia consisting of stibnite (Sbn) and angular to rounded quartz (Qz) fragments of various sizes; (d) A fragment of semi-transparent quartz (Qz) with stibnite (Sbn) cemented by saccharoidal quartz (Qz) containing disseminated stibnite (Sbn). A vague is filled with barite (Brt) euhedral crystals covered by reddish Fe-oxides (Fe-ox.); (e) Stibnite (Sbn) filling cracks in quartz (Qz); (f) A silicified pod from two-mica gneiss including stibnite (Sbn) and rounded quartz (Qz) grains.

	Shear zone	Two-mica gneiss	Supergene oxidation
<b>Alteration minerals</b>	<b>Sericitization-silicification</b>		
Quartz		—————	
Sericite	—————	—————	
Rutile		—————	
<b>Gangue Minerals</b>			
Quartz	—————		
Barite	—————		
Ankerite		—————	
<b>Ore Minerals</b>			
Stibnite	—————	—————	
Berthierite	—————		
Sphalerite		—————	
Pyrite	—————	—————	
Chalcopyrite	—————	—————	
Native antimony	—————		
Arsenopyrite	—————		
<u>Wolframite</u>	—————		
Galena	—————		
<u>Marcasite</u>	—————		
<u>Pyrrhotite</u>	—————		
<u>Realgar</u>	—————		
Tetrahedrite	—————		—————
Native arsenic	—————		
<u>Native gold</u>	—————		
Valentinite			—————
Goethite			—————
Claudetite			—————

**Figure 8.** Alteration, gangue and ore minerals of the Sb-mineralization located at “Tas-Kapou”. The underlined ore minerals are described by Dimou [32] occurring as traces in the stibnite ore. They are included here for consistency. Line thickness depicts the relative abundances of the minerals.

Microscopically, stibnite is characterized by strong bireflectance and by complex pressure lamellae as a result of deformation (Figure 9a). It forms intergrowths with quartz. In the massive form, it appears cementing euhedral quartz, forming disseminations in quartz and filling cavities and interstices in quartz (Figure 9a–d). Acicular stibnite occurs as overgrowths on quartz. Minor chalcopyrite, sphalerite and pyrite, not exceeding <700 µm in width, are found in cavities in stibnite masses (Figure 9b,d). Euhedral pyrite (<400 µm in width) and arsenopyrite (<200 µm in width) are found in quartz (Figure 9d,e). Locally, aggregations of euhedral pyrite showing cataclasis occur in angular quartz grains where ankerite is present in cavities (Figure 9f).

Berthierite, barite and native antimony are found as inclusions (<100 µm in width) in stibnite and quartz, while valentinite (<50 µm in width) occurs in association with stibnite and berthierite (Figure 10a,b). Locally, sphalerite (<300 µm) is rimmed by ankerite and contains tetrahedrite inclusions, while claudetite and native arsenic occur closely related in quartz (Figure 10c).

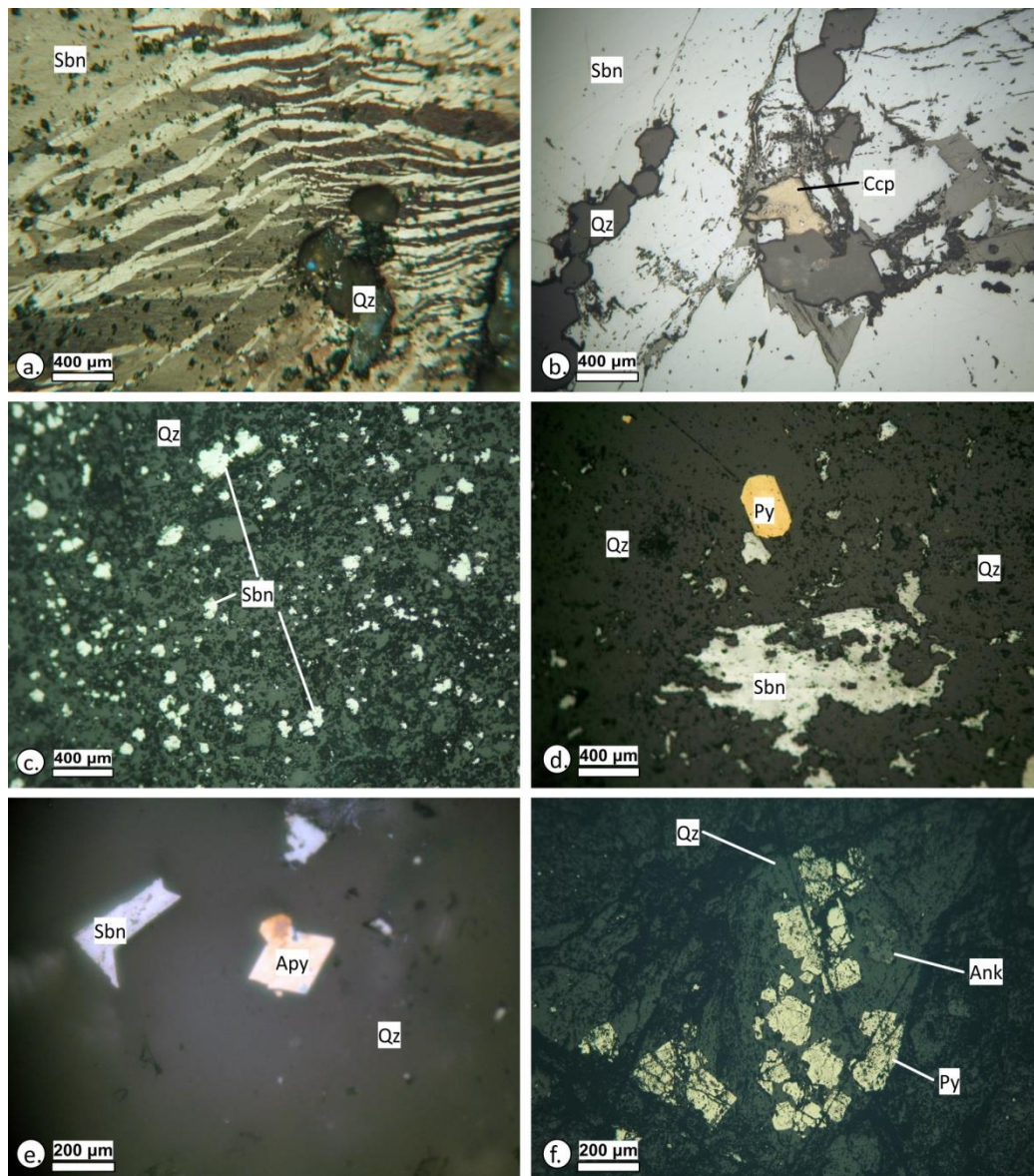


**Figure 9.** Photomicrographs of the stibnite mineralization from Rizana, under plane reflected light (Nichols crossed: (a), Nichols parallel: (b–f)): (a) Massive stibnite (Sbn) showing pressure lamellae and quartz (Qz); (b) Massive stibnite (Sbn) cementing euhedral quartz (Qz). Chalcopyrite (Ccp) occurs in stibnite; (c) stibnite (Sbn) as disseminations in quartz (Qz); (d) Stibnite (Sbn) fills a cavity in quartz (Qz), where also euhedral pyrite (Py) is found; (e) Stibnite (Sbn) filling interstices and euhedral arsenopyrite (Apy) in quartz (Qz); (f) Euhedral pyrite (Py) showing cataclasis in quartz (Qz) grains, where ankerite (Ank) also occurs in a cavity.

Berthierite, barite and native antimony are found as inclusions (<100  $\mu\text{m}$  in width) in stibnite and quartz, while valentinite (<50  $\mu\text{m}$  in width) occurs in association with stibnite and berthierite (Figure 10a,b). Locally, sphalerite (<300  $\mu\text{m}$ ) is rimmed by ankerite and contains tetrahedrite inclusions, while claudetite and native arsenic occur closely related in quartz (Figure 10c).

Quartz is the predominant gangue mineral related to the mineralization and appears semi-transparent to saccharoidal (Figures 7b–e and 8). Hydrothermal brecciation resulted in the intense fragmentation of quartz and grain reduction. Angular and rounded quartz fragments may coexist (Figure 7c), while the presence of micro-brecciated quartz is also common (Figure 7b). Acicular stibnite (<2 cm in width), as well as euhedral pyrite (<500  $\mu\text{m}$

in width) and arsenopyrite (<200 µm in width) are hosted in quartz (Figure 9c,d). Locally, cavities in quartz are filled with euhedral barite, which is stained by Fe-oxides due to oxidation (Figure 7d).

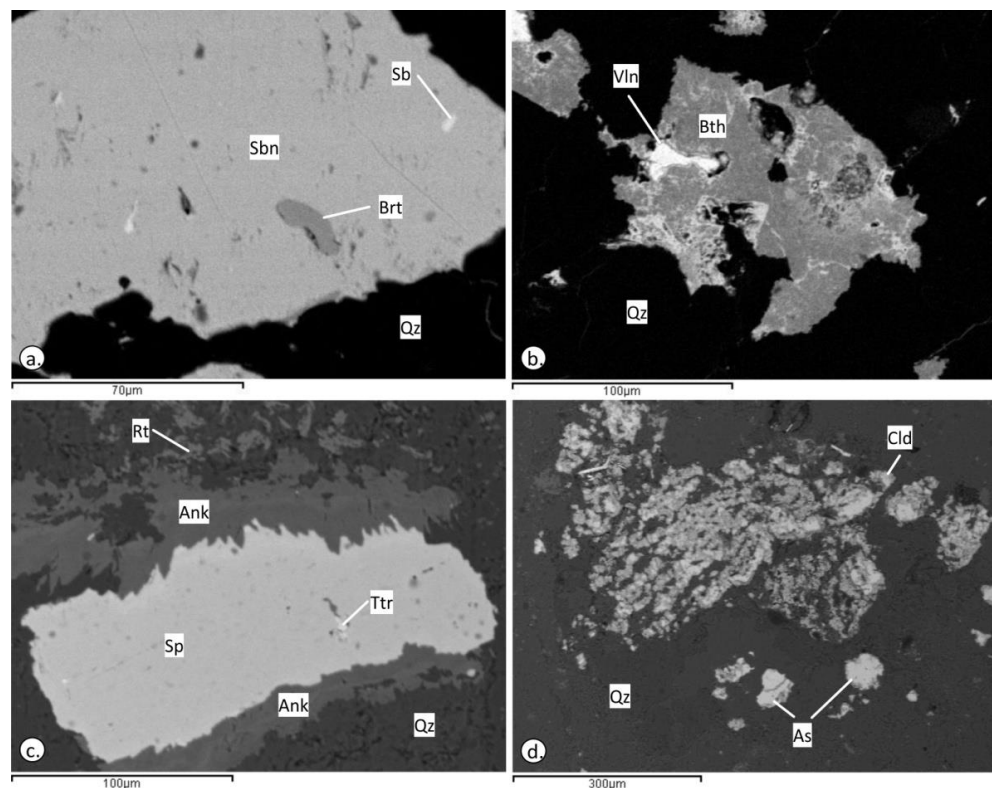


**Figure 10.** SEM back-scattered electron images of the stibnite mineralization: (a) Stibnite (Sbn) bearing barite (Brt) and native antimony (Sb) in quartz (Qz); (b) Berthierite (Bth) fills a cavity in quartz (Qz) and is oxidized to valentinite (Vln); (c) Sphalerite (Sp) is rimmed by ankerite (Ank) and includes tetrahedrite (Ttr). The ground mass includes quartz (Qz) and rutile (Rt); (d) Claudetite (Cl) and native arsenic (As) fill cavities in quartz (Qz).

#### 4.3. Mineral Chemistry

The mineral formulas of stibnite, pyrite, sphalerite, chalcopyrite, berthierite and valentinite, calculated by SEM-EDS analysis, are summarized in Table 2 (see also Supplementary Table S2). Locally, As (<0.15 wt.%) and Zn (<0.07 wt.%) were measured in stibnite, Cu (<0.07 wt.%) and Ni in pyrite and Mn (<0.16 wt.%) in sphalerite (Supplementary Table S2). Berthierite contains As (<2.02 wt.%) and traces of Cu (<0.31 wt.%), Zn (<0.25 wt.%) and Ag (<0.17 wt.%), while valentinite includes Zn (<0.82 wt.%), Fe (<0.50 wt.%), Ag (<0.13 wt.%) and Cu (<0.04 wt.%) (Supplementary Table S2). Specific correlation trends that could indicate substitution trends are not documented for Fe vs. Sb in stibnite and for As vs. Sb in berthierite.

**Table 2.** SEM-EDS analysis and mineral formulas of stibnite, pyrite, sphalerite and chalcopyrite.

Mineral	Mineral Formulas
Stibnite	$Sb_{1.87}As_{0.01}Cu_{0.03}Fe_{0.05}S_{3.03}-Sb_{1.93}S_{3.07}$
Pyrite	$Fe_{0.99}Co_{0.01}S_{2.00}-Fe_{0.99}S_{2.01}$
Sphalerite	$Zn_{0.86}Fe_{0.07}Cd_{0.01}S_{1.06}-Zn_{0.92}S_{1.08}$
Chalcopyrite	$Cu_{0.88}Fe_{0.99}S_{2.13}-Cu_{0.88}Fe_{0.95}As_{0.01}S_{2.16}$
Berthierite	$Fe_{1.15}Sb_{1.78}As_{0.11}Zn_{0.02}Cu_{0.02}Ag_{0.01}S_{3.92}-Fe_{1.05}Sb_{1.79}As_{0.11}S_{4.05}$
Valentinite	$Sb_{1.94}Zn_{0.04}Fe_{0.03}O_{2.99}-Sb_{1.97}O_{3.03}$

#### 4.4. Host Rock Geochemistry

Bulk rock geochemical analyses of sericitized two-mica gneiss (RZN04), silicified two-mica gneiss containing minor stibnite (RZN05), and sericitized and oxidized two-mica gneiss (RZN08) were conducted in order to investigate their trace element endowment. Table 3 summarizes the trace elements used in an attempt to compare the geochemical profiles of the analyzed samples with those of previously published two-mica gneiss samples [36] (Supplementary Table S1). Based on mobile and immobile element availability, two multi-element discrimination diagrams were produced normalized after primitive mantle [52] and after upper continental crust [53] (Figure 11a,b). The complete analytical datasets are given in Supplementary Table S1.

**Table 3.** Bulk geochemical analyses of two-mica gneiss from the Sb-mineralization at Rizana. For the full list of the geochemical analyses, see Table S1 at Supplementary Materials.

	Two-Mica Gneiss		
	Sericitized	Silicified with Stibnite	Sericitized and Oxidized
	RZN04	RZN05	RZN08
wt.%			
K	1.6	1.2	0.05
Ti	0.6	0.26	1.3
ppm			
Ba	234	291	781
Ce	32	37	23
La	12	17	10
Nb	8.4	4.4	5.1
P	1139	1884	1160
Pb	18	32	3.9
Rb	60	64	3.1
Sr	1638	2670	867
Th	4.4	4.7	0.7
Y	12	6.1	39
Zr	1.6	4.8	6.5

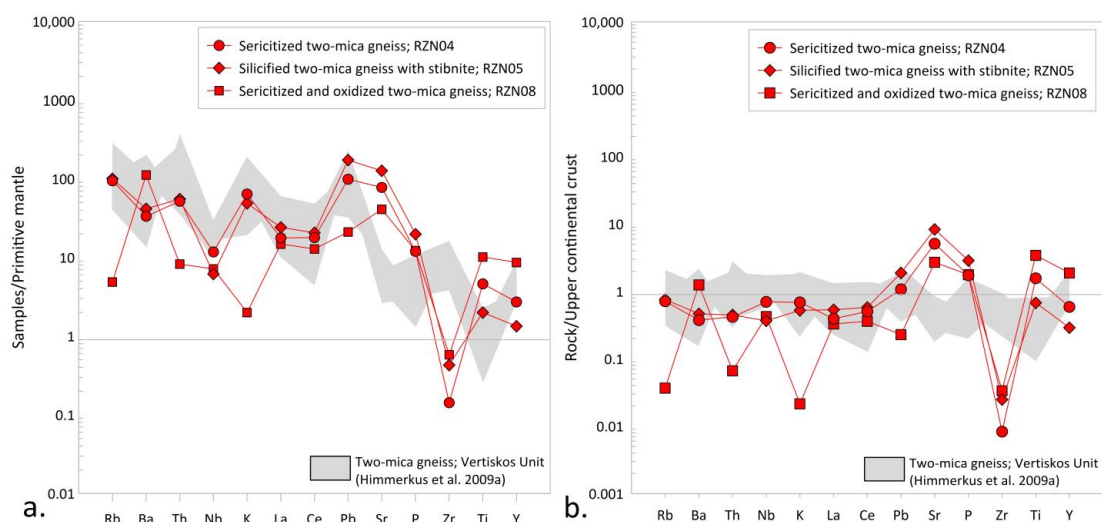


**Figure 11.** Primitive mantle (a) and upper continental crust (b) normalized logarithmic spider diagrams of three sericitized and/or silicified two-mica gneiss analyzed in the present study and the plot areas (gray shaded) of the reference two-mica gneiss from the Vertiskos Unit sourced by [36] (primitive mantle and upper continental crust normalized values after [52] and after [53], respectively).

Trace elemental concentrations of samples RZN04 and RZN05 are similar but vary significantly in sample RZN08 (Figure 11a,b). Sample RZN05 is the most enriched in

P (<1884 ppm) and Sr (<2670 ppm), while sample RZN08 in Ba (<781 ppm) (Table 3). The geochemical profiles of samples RZN04 and RZN05 for the elements Rb, Ba, Th, Nb, K, La, Ce and Pb largely overlap the reference plot area, while the geochemical profile of sample RZN08 exhibits distinct variations compared both to samples RZN04 and RZN05, as well as to the plot area of the reference two-mica gneiss (Figure 11a,b). All the analyzed samples are significantly enriched in Sr, while Ti is more enriched in samples RZN05 and RZN08 (<1.3 wt.% in RZN08) in respect to the reference two-mica gneiss (Figure 11a,b). Sample RZN08 is depleted in Rb, Th and K, while an extensive Zr depletion is shown for all the analyzed samples (Figure 11a,b).

#### 4.5. Bulk Ore Geochemistry—Critical Metal Contents

Bulk geochemical analysis of the stibnite mineralization was conducted in order to investigate their endowment trace elements. Selected base metals (As, Cu, Mn, Mo, Ni, Pb, Zn) and critical metals of the analyzed stibnite vein samples (RZN03a, RZN03b, RZN07) are summarized in Table 4 and reveal distinct enrichments and depletions in trace elements (Table 4; Figure 12). For comparison, bulk geochemical analyses of the stibnite mineralization from Gerakario were considered [8] (Table 4; Figure 12). Additionally, the plot area of the available critical elements from the two-mica gneiss of the Vertiskos Unit, published by Himmerkus et al. [36], is shown in Figure 12.

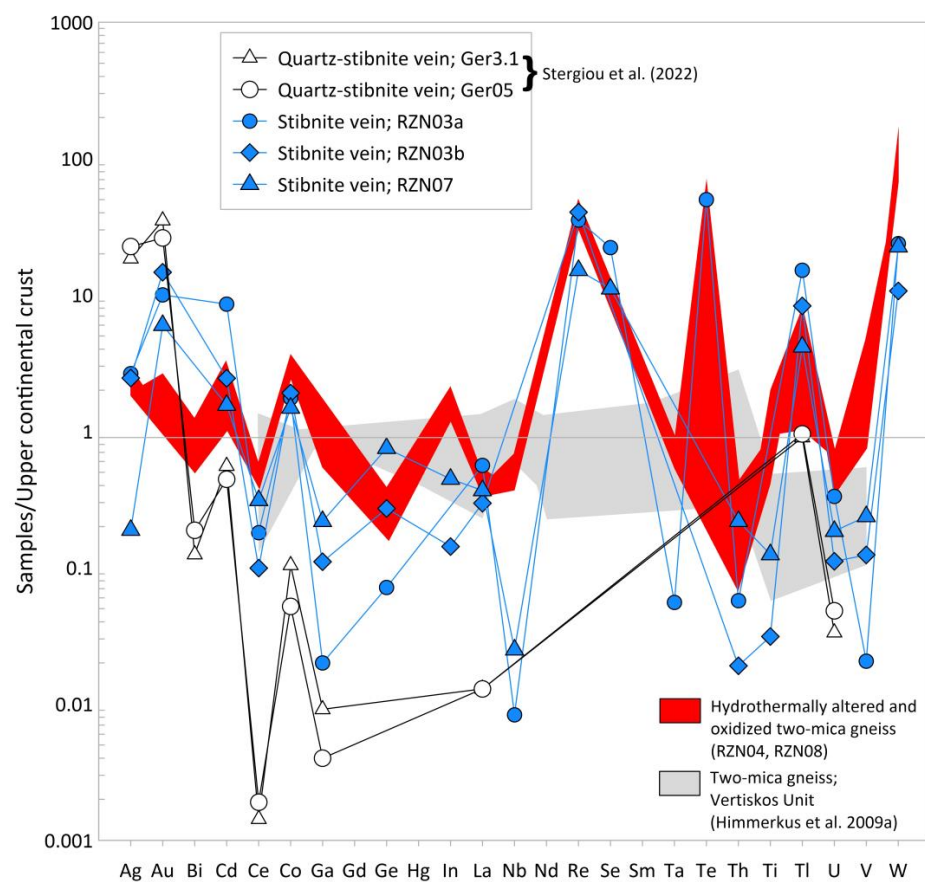


**Figure 12.** Upper continental crust normalized logarithmic spider diagram of selected critical metals from the three stibnite vein samples analyzed in this study compared to the stibnite mineralization from Gerakario (after Stergiou et al. [8]) and to the plot area of the analyzed two-mica gneiss (red shaded). The plot area (gray shaded) of the reference two-mica gneiss from the Vertiskos Unit published by Himmerkus et al. [36] is also shown for comparison (Upper continental crust normalized values after [53]).

**Table 4.** Bulk ore geochemical analyses of selected base and critical metals from the Rizana and Gerakario stibnite mineralization [8]. Please see Table S1 in the Supplementary Materials for the full geochemical dataset.

	Rizana						Gerakario	
	Sericitized Two-Mica Gneiss	Silicified Two-Mica Gneiss with Stibnite	Sericitized and Oxidized Two-Mica Gneiss	Stibnite Mineralization			Stibnite Mineralization	
	RZN04	RZN05	RZN08	RZN03a	RZN03b	RZN07	Ger3.1	Ger05
ppm								
Ag	0.16	0.1	0.1	0.14	0.13	0.01	0.98	1.2
As	113	>10,000	1140	1108	1205	1282	6.2	4.6
Au	b.d.l.	0.004	b.d.l.	0.02	0.02	0.009	0.05	0.04
Bi	0.08	0.17	0.2	b.d.l.	b.d.l.	b.d.l.	0.02	0.03
Cd	0.09	0.12	0.3	0.77	0.22	0.14	0.05	0.04
Ce	32	37	23	11	6.2	20	0.09	0.12
Co	48	63	43	30	33	26	1.8	0.9
Cu	40	25	61	495	14	7.8	27	31
Ga	21	9.8	21	0.35	1.9	3.8	0.16	0.07
Gd	n.a.	n.a.	n.a.	n.a.	n.a.	n.a.	<0.05	<0.05
Ge	0.47	0.22	0.54	0.1	0.38	1.1	<0.05	<0.05
Hg	n.a.	n.a.	n.a.	n.a.	n.a.	n.a.	<0.005	<0.005
In	0.08	0.07	0.12	b.d.l.	0.01	0.03	<0.005	<0.005
La	12	17	10	17	9.2	11	0.4	0.4
Mn	1771	545	2317	6	<5	212	35	20
Mo	0.93	1.7	5.7	0.35	0.2	0.86	0.12	0.09
Nb	8.4	4.4	5.1	0.1	b.d.l.	0.3	<0.05	<0.05
Ni	63	75	137	5.3	4.6	9.4	5.9	3.6
Nd	n.a.	n.a.	n.a.	n.a.	n.a.	n.a.	<0.1	<0.1
Pb	18	32	3.9	86	33	42	22	20
Re	0.006	0.01	0.007	0.007	0.008	0.003	<0.001	<0.001
Sb	198	3851	1059	>10,000	>10,000	>10,000	326,000	574,000
Se	b.d.l.	b.d.l.	b.d.l.	2	b.d.l.	b.d.l.	<0.2	<0.2
Sm	n.a.	n.a.	n.a.	n.a.	n.a.	n.a.	<0.03	<0.03
Ta	0.82	0.48	0.49	0.05	b.d.l.	b.d.l.	<0.01	<0.01
Te	0.08	0.14	b.d.l.	0.1	b.d.l.	b.d.l.	<0.01	<0.01
Th	4.4	4.7	0.7	0.6	0.2	2.3	<0.2	<0.2
Ti	6000	2600	13,200	b.d.l.	200	800	<0.005	<0.005
Tl	0.92	7.5	1.2	14	7.5	3.8	0.81	0.86
U	1.7	0.9	2	0.9	0.3	0.5	0.09	0.13
V	178	72	465	2	12	23	<1	<1
W	130	331	125	45	20	43	<0.05	<0.05
Zn	122	54	201	15	10	28	6	b.d.l.
Ag: Au	null	25	null	7	6.5	1.1	20	30

Abbreviations: b.d.l. = below detection limit; n.a. = not analyzed; null = incalculable.

Most of the base metals are relatively more enriched in the hydrothermally altered and oxidized two-mica gneiss samples compared to the stibnite vein samples both from Rizana and Gerakario (Table 4). The highest enrichment in As (>10,000 ppm) was detected in sample RZN05, while Mn (2317 ppm), Mo (5.7 ppm), Ni (137 ppm) and Zn (201 ppm) contents are more enriched in sample RZN08. In contrast, Cu (<495 ppm) and Pb (<86 ppm) are more enriched in the stibnite vein samples (Table 4).

The stibnite vein samples from Rizana and the hydrothermally altered and oxidized two-mica gneiss samples exhibit specific enrichments in critical metals compared to the reference two-mica gneiss from the Vertiskos Unit (Figure 12). In addition, the stibnite vein samples from Rizana are more enriched in critical metals compared to the stibnite vein samples from Gerakario (Figure 12).

The highest contents of critical metals in the stibnite mineralization from Rizana include Cd (<0.77 ppm), Re (<0.008 ppm), Se (2 ppm) and Tl (<14 ppm) (Table 4; Figure 12). The stibnite mineralization from Gerakario incorporates the highest contents of Ag (<1.2 ppm) and Au (<0.05 ppm) (Table 4; Figure 12). The hydrothermally altered and oxidized two-mica gneiss from Rizana is more enriched in Co (<63 ppm), Ga (<9.8 ppm), In (<0.12 ppm), Te (<0.14 ppm) and W (<331 pm) (Table 4; Figure 12). The trace elemental contents of Ce,

Ga, Ge, In, La, Nb, Ta, Th, Ti, U and V—which are plotted in or below the plot area of the reference two-mica gneiss of Vertiskos Unit—are noteworthy (Figure 12).

#### 4.6. Fluid Inclusions Study

Fluid inclusions in quartz veins with the stibnite mineralization at Rizana were studied in order to clarify the conditions of formation of the mineralization, e.g., temperature, and composition of the fluids. Quartz is anhedral with a polygonal shape and has a white color. The polygonal shape is attributed to the quartz recrystallization, caused by multiple and continuous flow of the hydrothermal fluids. This process obliterated a large number of fluid inclusion assemblages, and for this reason, many parts of the veins are free of inclusions [54]. Consequently, the microthermometric measurements were restricted in parts of the veins, where recrystallization did not significantly affect the quartz (Figure 13a). No fluid inclusions were identified along the quartz growth zones.

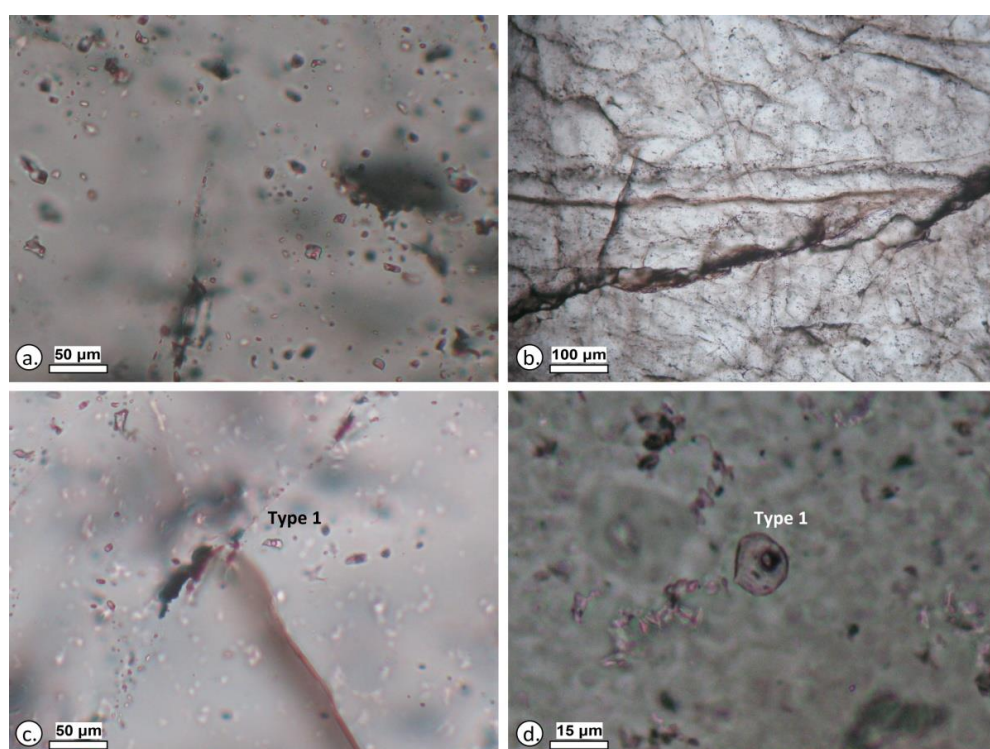


**Figure 13.** Fluid inclusions in quartz from the stibnite mineralization at Rizana: (a) Clusters of fluid inclusions where recrystallization did not significantly affect the quartz; (b) Secondary inclusions of very small size (<1  $\mu\text{m}$ ) along healed fractures in the quartz; (c,d) Two-phase fluid inclusions of type 1.

Microthermometric measurements were performed on 37 primary fluid inclusions. These inclusions are considered primary based on the criteria proposed by Roedder [55], Goldstein and Reynolds [56], and Bodnar [57]. The size of the inclusions is relatively small and reaches up to 12  $\mu\text{m}$ . Secondary inclusions along healed ruptures were also detected (Figure 13b), but their dimensions were too small for microthermometry. Based on the phase ratios in the inclusions at room temperature and their behavior during microthermometry (heating and cooling), one type of primary fluid inclusions was identified (Type 1). They consist of a liquid water phase and a vapor bubble that occupies 20–30% of the volume of the inclusion (Figure 13c,d). During heating the inclusions were homogenized into the liquid phase.

The initial melting temperatures of ice ( $T_e$ ) in the fluid inclusions, during cooling, were about  $-21.3\text{ }^\circ\text{C}$ , indicating that the only salt present in the fluids was NaCl (Shepherd et al., 1985). The final ice melting temperatures ( $T_m$ ) of the inclusions ranged

from  $-5.2$  to  $-4.0$  °C, indicating a low to slightly moderate salinity of 6.6 to 8.1% wt. eq. NaCl in the  $H_2O$ -NaCl system, according to Roedder [55], Potter et al. [58] and Shepherd et al. [59]. During heating the fluid inclusions homogenized into the liquid phase, at temperatures (Th) from 217 to 254 °C (Figure 14).

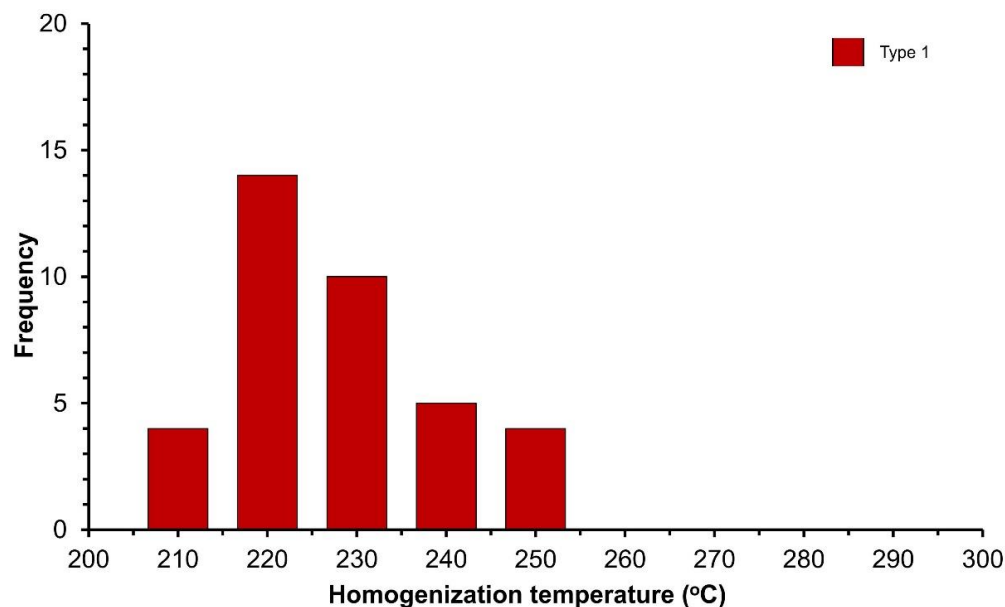


**Figure 14.** Histogram showing the homogenization temperatures of Type 1 fluid inclusions in quartz from the stibnite Rizana mineralization.

## 5. Discussion

During recent years an increasing number of studies have been focused on the investigation of the critical metals endowment of the Cenozoic magmatic-hydrothermal deposits and related mineralization hosted in the Vertiskos Unit and the adjacent Rhodope Unit in northern Greece (e.g., [60–63]).

The intrusion related mineralization in the Vertiskos Unit includes veins hosted in shear-zones and metamorphic rocks [20] (Figure 1). Based on the main metal commodities, these deposits could be subdivided in polymetallic (Cu-As-Pb-Bi-Au-Te)-enriched and in Sb-enriched. The first category of deposits incorporate varying concentrations of Bi and Te as Bi-sulfosalts and/or tellurides associated with Au and Ag [64,65]. It has been suggested that the formation of this mineralization is related to concealed proximal and/or distal magmatic intrusions and magmatic-hydrothermal mineralizing processes set along or near shear-zones under retrograde greenschist facies metamorphism [66,67]. In the polymetallic vein mineralization at Laodikino, pilsenite and altaite are found in chalcopyrite and galena, respectively, while tetrahedrite includes up to 7185 ppm of Ag [64–68]. In Koronouda, joseite-B, pilsenite, tellurobismuthite and hessite form intergrowths, whereas up to 28.3 ppm of Au is hosted in the quartz veins [64,69]. In the quartz veins at Drakontio, aikinite, matildite and emplectite are associated with 22.5 ppm of Au [70]. In addition, argentopentlandite is found in Greece only in the quartz veins at Koronouda and Stefania-Paliomylos [71,72].

The three major Sb-vein deposits located at Gerakario, Philadelphio and Rizana are characterized by differences in mineralogy and geochemistry in respect to the rest of the vein-type deposits found in the Vertiskos Unit (Figure 1). Antimony found as stibnite is the dominant commodity, while base metal (i.e., Cu, Zn, Pb) contents are significantly diminished as sulfides such as pyrite, chalcopyrite, sphalerite and galena are minor constituents of the ore assemblage ([8,30,32], this study). In addition, low contents of Bi, Te, Au and Ag are documented for the Sb-vein deposits (Table 4). Bismuth and Te bearing sulfosalts are not reported for the ore assemblages at Gerakario, Philadelphio and Rizana, while the highest Bi (<0.03 ppm in Ger05) and Te (<0.1 ppm in RZN03b) contents measured from

Rizana and Gerakario are lower or close to those of the hydrothermally altered two-mica gneiss ([8,30,32], this study) (Table 4, Figure 12). Furthermore, despite native gold being mentioned as occurring in the Sb-vein deposits [30,32], the highest measured Au contents (<0.05 in Ger3.1) are notably restricted. The same is observed for Ag (<0.98 ppm in Ger3.1).

In terms of anatomy, all the Sb-vein deposits are structurally controlled. Nevertheless, the Gerakario deposit occurs peripheral to a Cu–Au porphyry deposit, while the deposits at Rizana and Philadelphia are associated with relatively wide (<8 m in Rizana) brittle shear-zones. At Rizana, the slightly altered and mineralized rhyodacite outcrop, distancing 2 km from the Sb-mineralization (Figure 2), could be related to the mineralizing processes. The Rizana rhyodacite is an example of the Cenozoic magmatism in the Vertiskos Unit [42]. This magmatism produced several magmatic rocks restricted in volume and usually concealed, although able to contribute with magmatic fluids and to raise the thermal gradients inducing fluid circulation [64,67].

In terms of mineralogy, the ore assemblages at Rizana and Gerakario differ from the one at Philadelphia. Besides stibnite, Sb-sulfosalts (berthierite, tetrahedrite), Sb-oxides (valentinite at Tas-Kapou and cervanite, stibiconite at Pilaf Tepe) and native antimony are found at Rizana, while at Gerakario only berthierite and native antimony are reported ([8,32], this study). In contrast, the Sb-mineralization at Philadelphia is more complex including sulfosalts (chalcostibite, tetrahedrite, zinkenite), oxysulfides (kermesite) and oxides (stibiconite) [30].

On the basis of the available geochemical data, further differences occur between the Sb-vein deposits at Rizana and Gerakario. The Sb-mineralization at Rizana is relatively more enriched in metals including Cu, Mo, Ni, Pb and Zn, compared to the Gerakario Sb-mineralization (Table 4). Arsenic is significantly more enriched at Rizana (<1282 ppm in RZN07 and >10,000 ppm in RZN05) associated with the occurrence of arsenopyrite, claudetite and native As (Table 4, Figure 10d). In addition, As is found in stibnite (<0.35 wt.%), chalcopyrite (<0.61 wt.%) and berthierite (<2.02 wt.%), while its contents are below detection limits in pyrite, sphalerite and valentinite (Supplementary Table S2). The fact that no specific correlation was documented for As vs. Sb in berthierite, suggesting the random incorporation of As in berthierite, is noteworthy. Furthermore, critical metals, including W (<45 ppm), Tl (<14 ppm) and Cd (<0.77 ppm), are more enriched in the Sb-mineralization at Rizana compared to those measured for Gerakario (Figure 12). The described mineralogical and geochemical differences indicate diverse physico-chemical conditions for the Sb-mineralization in the Vertiskos Unit.

Based on the fluid inclusions study, the stibnite ore bodies at Rizana were formed in a restricted range of temperatures and salinities, during cooling and pressure decrease. The fluids were determined to be NaCl-dominated according to the very close eutectic temperatures of the NaCl–H<sub>2</sub>O system, had low to slightly moderate salinities (6.6 to 8.1 wt.% eq. NaCl) and had homogenization temperatures from 217 to 254 °C, with a maximum of 220 °C (Figure 14). These conditions indicate a hydrothermal event that resulted from the mixing of magmatic-hydrothermal fluids with meteoric water, a process which may cause the formation of sulfide mineralization. Such processes have been previously described by Demir et al. [73,74].

Further, by taking into consideration the ore assemblage where typical high-sulfidation minerals, such as enargite and luzonite, are missing, the high Ag: Au ratio (=1.1–7.0), the barite occurrence as gangue mineral and the Ba contents (<98 ppm in the Sb-mineralization; sample RZN07), and the variable Fe contents in sphalerite (=0.19–4.29 wt.%), low- to intermediate-sulfidation fluid conditions could be assumed for the mineralizing fluids (cf. Table 4, Supplementary Tables S1 and S2, [75]).

The fluid inclusions study of the epithermal quartz–stibnite veins at Gerakario has shown that the Sb-mineralization was formed from fluids with slightly higher salinities (8 to 10 wt.% NaCl equiv.) and temperatures (280–320 °C) compared to those measured for Rizana [8].

The Sb-mineralization at Rizana is more enriched in terms of mineralogy and geochemistry compared to the Gerakario stibnite mineralization. At Rizana, this could be related to the extensive interaction between the mineralizing fluids and the wall-rocks, as well as to the combined ability of Sb and As to form compounds and to act as metal carriers [76]. The hydrothermally altered (sericitization and silicification) two-mica gneiss host rocks further indicate the extent of the fluid and wall-rock interaction, set under acidic and pervasive conditions (Figure 3a). Strontium (<2670 ppm) and P (<1884 ppm) are enriched in the analyzed two-mica gneiss samples (Figure 11). The hydrothermal alteration of K-feldspar and plagioclase may be related to the elevated Sr contents, while P contents could be ascribed to the alteration of apatite.

Following the categorization made by Dill [11] for the Sb-mineralization occurring in subduction-related systems, and by taking into consideration the structural setting, the ore mineralogy and geochemistry, and the fluid inclusion study of the Sb-mineralization at Rizana, it could be suggested that the mineralization belongs to Type III. This type is described as transitional between Type I (i.e., shear-zone-hosted; low to very low grade metamorphism; mineralizing fluids related to deep crustal devolatilization) and Type II (i.e., stock-work veins; epithermal mineralizing conditions associated with acidic to intermediate subvolcanic to volcanic rocks) and forms composite vein-type deposits [11]. According to Dill [11], the contents of Bi, Ag, As and Hg are diagnostic in distinguishing between Type I (i.e., poor in Bi, Ag, As); Type II (i.e., anomalously enrichments in Bi, Ag, As, Hg); and Type III (i.e., element contents vary according to the distance of the magmatic rocks). Arsenic contents (1108–1282 ppm) of the stibnite ore and those of the silicified two-mica sample (RZN05: >10,000 ppm), as well as the close occurrence of the Miocene Rizana rhyodacite, could support that the stibnite mineralization at Rizana belongs to Type III. Furthermore, the Sb-mineralization at Rizana bears no similarity to the major Sb-deposits located at the northern part of the SMMB, extending from Serbia to North Macedonia, and hosted in volcanic and sedimentary rocks [14–18]. Thallium mineralogy and geochemistry, and enrichments in Se and Hg, are profound differences between these deposits and the deposit at Rizana.

It should also be mentioned that, in order to further understand the mineralizing processes at Rizana, the geochemical enrichment in tungsten and the presence of wolframite as a minor constituent in the Sb-mineralization at Tas-Kapou, in relation with the W–Sb-mineralization occurring nearby at Pilaf-Tepe, needs further investigation. Vasilatos et al. [33] describe that stibnite occurs in brecciated masses of Fe–wolframite (ferberite:  $\text{FeWO}_4$ ) and further mention that W and Sb are not geochemically correlated at Pilaf-Tepe. Thus, it could be suggested that, at Rizana, a distinct mineralizing stage enriched in W preceded the later Sb-introducing stage. Similar mineralizing processes have been described for various mesothermal to epithermal Sb–W±Au mineralization globally (e.g., [5,77]). Nevertheless, wolframite (including both huebnerite:  $\text{MnWO}_4$ ; and ferberite:  $\text{FeWO}_4$ ) has also been reported as occurring at Baia Sprie (Romania), formed under epithermal conditions (i.e., low temperatures: 154–240 °C, and low salinities: 4.6–6.4 wt.% NaCl equiv.) related to subvolcanic–volcanic activity and extensive mixing between magmatic fluids and meteoric water [78].

Future investigations at Rizana, aiming to clarify the regional metallogenic model, should be focused on tungsten mineralogy, geochemistry and possibly on wolframite fluid inclusions study. Additionally, data on Tl–Se–Hg geochemistry and mineralogy could further illuminate the physico-chemical conditions during the formation of the Sb-mineralization.

## 6. Conclusions

1. The Sb-vein deposit at Rizana is hosted by a NE–SW-trending brittle shear-zone, crosscutting the two-mica gneiss and augen-gneiss of the Vertiskos Unit.
2. The ore bodies form veins and discordant lodes, exhibiting massive and brecciated textures.

3. The ore assemblage contains stibnite + berthierite + sphalerite + pyrite + chalcopyrite + native antimony, traces of wolframite, arsenopyrite, galena, marcasite, pyrrhotite, realgar, tetrahedrite, native As and native Au, while quartz and minor ankerite and barite are the gangue minerals. Oxidation minerals include valentinite, goethite and claudetite.
4. Sericitization and silicification of moderate intensities have affected the two-mica gneiss and formed spatially restricted hydrothermal halos. Noteworthy are the significantly enriched concentrations of As, Mn, W and Zn in the analyzed two-mica gneiss reflecting metal remobilization under oxidation.
5. The Miocene Rizana rhyodacite, which outcrops in the study area, is sericitically altered, contains pyrite disseminations and seems to be related to the Sb-mineralization.
6. Bulk ore geochemistry revealed low to moderate enrichments in respect to the hydrothermally altered and oxidized two-mica gneiss, mainly related to Au, Cd, Se and Tl.
7. The study of the fluid inclusions showed that the mineralization was formed by fluids with low to slightly moderate salinities (6.6–8.1 wt% NaCl equiv) at relatively low homogenization temperatures (217–254 °C, with a maximum at 220 °C).
8. The discussed Sb-vein deposits in the Vertiskos Unit are characterized by significant differences. The quartz–stibnite veins at Gerakario refer to a minor and regionally sole example of Sb-mineralization occurring in the periphery of a porphyry system. In contrast, the major Sb-vein deposit at Rizana is well set in a relatively wide brittle shear-zone. Fluids produced after the extensive mixing of hydrothermal fluids with meteoric water were able to accumulate and transfer metals along the brittle shear-zone and deposit the mineralization under low- to intermediate-sulfidation and transitional mesothermal to epithermal conditions.

**Supplementary Materials:** The following supporting information can be downloaded at: <https://www.mdpi.com/article/10.3390/geosciences13020061/s1>, Table S1: Bulk geochemistry, Table S2: Mineral formulas.

**Author Contributions:** Conceptualization, V.M.; methodology, V.M.; software, C.L.S.; formal analysis, E.S., C.L.S. and L.P.; data curation, E.S. and C.L.S.; writing—original draft preparation, C.L.S. and V.M.; writing—review and editing, P.V., L.P., N.K., G.-A.S., L.P. and E.S.; visualization, C.L.S. and E.S.; supervision, V.M. All authors have read and agreed to the published version of the manuscript.

**Funding:** This research received no external funding.

**Data Availability Statement:** The data presented in this study are available in the article. The data presented in this study are available within the article and in the Supplementary Tables S1 and S2.

**Acknowledgments:** The authors would like to acknowledge Aris Stamatidis for the preparation of the thin-polished and polished sections. Three anonymous reviewers are thanked for their fruitful comments and revisions that significantly improved the initial manuscript, as well as the Assistant Editor for editorial handling.

**Conflicts of Interest:** The authors declare no conflict of interest.

## References

1. Anderson, C.G. The metallurgy of antimony. *Geochemistry* **2021**, *72*, 3–8. [[CrossRef](#)]
2. Schwarz-Schampera, U. Antimony. In *Critical Metals Handbook*; Gunn, G., Ed.; John Wiley & Sons: Hoboken, NJ, USA, 2014; pp. 70–98.
3. Hofstra, A.H.; Kreiner, D.C. *Systems-Deposits-Commodities-Critical Minerals Table for the Earth Mapping Resources Initiative*; Open-File Report 2020-1042; U.S. Geological Survey: Reston, VA, USA, 2020; p. 24.
4. Dill, H.G.; Pertold, Z.; Kilibarda, R.C. Sediment-hosted and volcanic-hosted Sb vein mineralization in the Potosi region, Central Bolivia. *Econ. Geol.* **1997**, *92*, 623–632. [[CrossRef](#)]
5. Dill, H.G.; Melcher, F.; Botz, B. Meso- to epithermal W-bearing Sb vein-type deposits in calcareous rocks in western Thailand; with special reference to their metallogenetic position in SE Asia. *Ore Geol. Rev.* **2008**, *34*, 242–262. [[CrossRef](#)]

6. Voudouris, P.; Mavrogonatos, C.; Spry, P.G.; Baker, T.; Melfos, V.; Klemd, R.; Haase, K.; Repstock, A.; Djiba, A.; Bismayer, U.; et al. Porphyry and epithermal deposits in Greece: An overview, new discoveries, and mineralogical constraints on their genesis. *Ore Geol. Rev.* **2019**, *107*, 654–691. [[CrossRef](#)]
7. Wang, L.; Qin, K.Z.; Song, G.X.; Li, G.M. A review of intermediate sulfidation epithermal deposits and subclassification. *Ore Geol. Rev.* **2019**, *107*, 434–456. [[CrossRef](#)]
8. Stergiou, C.L.; Melfos, V.; Voudouris, P.; Papadopoulou, L.; Spry, P.G.; Peytcheva, I.; Dimitrova, D.; Stefanova, E. A Fluid Inclusion and Critical/Rare Metal Study of Epithermal Quartz-Stibnite Veins Associated with the Gerakario Porphyry Deposit, Northern Greece. *Appl. Sci.* **2022**, *12*, 909. [[CrossRef](#)]
9. Fu, S.; Hu, R.; Bi, X.; Sullivan, N.A.; Yan, J. Trace element composition of stibnite: Substitution mechanism and implications for the genesis of Sb deposits in southern China. *Appl. Geochem.* **2020**, *118*, 104637. [[CrossRef](#)]
10. Zhou, Z.; Li, H.; Yonezu, K.; Imai, A.; Tindell, T. In-situ trace elements and sulfur isotopic analyses of stibnite: Constraints on the genesis of Sb/Sb-polymetallic deposits in southern China. *J. Geochem. Explor.* **2023**, *247*, 107177. [[CrossRef](#)]
11. Dill, H.G. Evolution of Sb mineralisation in modern fold belts: A comparison of the Sb mineralisation in the Central Andes (Bolivia) and the Western Carpathians (Slovakia). *Miner. Depos.* **1998**, *33*, 359–378. [[CrossRef](#)]
12. Cook, N.J.; Ciobanu, C.L.; Giles, D.; Wade, B. Correlating textures and trace elements in ore minerals. Mineral deposit research for a high-tech world. In Proceedings of the 12th Biennial SGA Meeting, Uppsala, Sweden, 12–15 August 2013.
13. Baker, T. Gold±copper endowment and deposit diversity in the Western Tethyan magmatic belt, southeast Europe: Implications for exploration. *Econ. Geol.* **2019**, *114*, 1237–1250. [[CrossRef](#)]
14. Janković, S. Sb-As-Tl Mineral Associations in the Mediterranean Region. *Inter. Geol. Rev.* **1989**, *31*, 262–273. [[CrossRef](#)]
15. Radosavljević, S.A.; Stojanović, J.N.; Radosavljević-Mihajlović, A.S.; Vuković, N.S. Rujevac Sb-Pb-Zn-As polymetallic deposit, Boranja orefield, Western Serbia: Native arsenic and arsenic mineralization. *Mineral. Petrol.* **2014**, *108*, 111–122. [[CrossRef](#)]
16. Palinkaš, S.S.; Hofstra, A.H.; Percival, T.J.; Šoštarkć, S.B.; Palinkaš, L.; Bermanec, V.; Pecskey, Z.; Boev, B. Comparison of the allchar Au-As-Sb-Tl deposit, Republic of Macedonia, with carlin-type gold deposits. In *Reviews in Economic Geology: Diversity of Carlin-Style Gold Deposits*; Cline, J.S., Ed.; Society of Economic Geologists: Littleton, CO, USA, 2018; pp. 335–363.
17. Đorđević, T.; Kolitsch, U.; Serafimovski, T.; Tasev, G.; Tepe, N.; Stöger-Pollach, M.; Hofmann, T.; Boev, B. Mineralogy and weathering of realgar-rich tailings at a former As-Sb-Cr mine at Lojane, North Macedonia. *Can. Mineral.* **2019**, *57*, 403–423. [[CrossRef](#)]
18. Mederski, S.; Pršek, J.; Majzlan, J.; Kiefer, S.; Dimitrova, D.; Milovský, R.; Koch, C.B.; Kozieñ, D. Geochemistry and textural evolution of As-Tl-Sb-Hg-rich pyrite from a sediment-hosted As-Sb-Tl-Pb±Hg±Au mineralization in Janjevo, Kosovo. *Ore Geol. Rev.* **2022**, *151*, 105221. [[CrossRef](#)]
19. Melfos, V.; Voudouris, P.C. Geological, mineralogical and geochemical aspects for critical and rare metals in Greece. *Minerals* **2012**, *2*, 300–317. [[CrossRef](#)]
20. Melfos, V.; Voudouris, P. Cenozoic metallogeny of Greece and potential for precious, critical and rare metals exploration. *Ore Geol. Rev.* **2017**, *89*, 1030–1057. [[CrossRef](#)]
21. Stergiou, C.L.; Melfos, V.; Voudouris, P. A Review on the Critical and Rare Metals Distribution throughout the Vertiskos Unit, N. Greece. In Proceedings of the 1st International Electronic Conference on Mineral Science at Sciforum, Basel, Switzerland, 16–31 July 2018.
22. McFall, K.A.; Naden, J.; Roberts, S.; Baker, T.; Spratt, J.; McDonald, I. Platinum-group minerals in the Skouries Cu-Au (Pd, Pt, Te) porphyry deposit. *Ore Geol. Rev.* **2018**, *99*, 344–364. [[CrossRef](#)]
23. Stergiou, C.L.; Melfos, V.; Voudouris, P.; Spry, P.G.; Papadopoulou, L.; Chatzipetros, A.; Giouri, K.; Mavrogonatos, C.; Filippidis, A. The geology, geochemistry, and origin of the porphyry Cu-Au-(Mo) system at Vathi, Serbo-Macedonian Massif, Greece. *Appl. Sci.* **2021**, *11*, 479. [[CrossRef](#)]
24. Stergiou, C.L.; Melfos, V.; Voudouris, P.; Papadopoulou, L.; Spry, P.G.; Peytcheva, I.; Dimitrova, D.; Stefanova, E.; Giouri, K. Rare and Critical Metals in Pyrite, Chalcopyrite, Magnetite, and Titanite from the Vathi Porphyry Cu-Au±Mo Deposit, Northern Greece. *Minerals* **2021**, *11*, 630. [[CrossRef](#)]
25. Arvanitidis, N.D. New metallogenetic concepts and sustainability perspectives for non-energy metallic minerals in Central Macedonia, Greece. *Bull. Geol. Soc. Greece* **2010**, *43*, 2437–2445. [[CrossRef](#)]
26. Tsirambides, A.; Filippidis, A. Metallic mineral resources of Greece. *Cent. Eur. J. Geosci.* **2012**, *4*, 641–650. [[CrossRef](#)]
27. Tsirambides, A.; Filippidis, A. Gold metallogeny of the Serbomacedonian-Rhodope metallogenic belt (SRMB). *Bull. Geol. Soc. Greece* **2016**, *50*, 2037–2046. [[CrossRef](#)]
28. Tsirambides, A.; Filippidis, A. Sb-Bi-bearing metallogeny of the Serbomacedonian-Rhodope metallogenic belt (SRMB). *Bull. Geol. Soc. Greece* **2019**, *55*, 34–64. [[CrossRef](#)]
29. Kanellopoulos, C.; Voudouris, P.; Moritz, R. Detachment-related Sb-As-Au-Ag-Te mineralization in Kallintiri area, northeastern Greece: Mineralogical and geochemical constraints. In *Proceedings XX Congress of the Carpathian-Balkan Geological Association*; Beqiraj, A., Ionescu, C., Christofides, G., Uta, A., Beqiraj Goga, E., Marku, S., Eds.; Buletini i Shkencave Gjeologjike: Tirana, Albania, 2014; pp. 162–165.
30. Cassard, D.; Bertrand, G.; Billa, M.; Serrano, J.J.; Tourlière, B.; Angel, J.M.; Gaál, G. ProMine mineral databases: New tools to assess primary and secondary mineral resources in Europe. In *3D, 4D and Predictive Modelling of Major Mineral Belts in Europe. Mineral Resource Reviews*; Weihed, P., Ed.; Springer: Cham, Switzerland, 2015; pp. 9–58.

31. Paraskevopoulos, G.M. The genesis of the wolframite and stibnite deposits at Lachanas, Central Macedonia. *Ann. Geol. Pays Hell.* **1958**, *9*, 227–241.
32. Dimou, E. Native minerals in rocks and mineralizations of Greece and their significance. *Bull. Geol. Soc. Greece* **1989**, *23*, 207–223.
33. Vasilatos, C.; Barlas, K.; Stamatakis, M.; Tsvivilis, S. Wolframite-stibnite mineral assemblages from Rizana Lachanas, Macedonia, Greece and their possible use as flux agent in the manufacturing of clinker. *Bull. Geol. Soc. Greece* **2001**, *34*, 827–834. [[CrossRef](#)]
34. Kakali, G.; Tsvivilis, S.; Kolovos, K.; Choupa, K.; Perraki, T.; Perraki, M.; Stamatakis, M.; Vasilatos, C. Use of secondary mineralizing raw materials in cement production. The case study of a stibnite ore. *Mater. Lett.* **2003**, *57*, 3117–3123. [[CrossRef](#)]
35. Skoupras, E. Study of the Stibnite Ore Mineralization in Rizana, Kilkis. Master's Thesis, Aristotle University of Thessaloniki, Thessaloniki, Greece, 2019.
36. Himmerkus, F.; Reischmann, T.; Kostopoulos, D. Serbo-Macedonian revisited: A Silurian basement terrane from northern Gondwana in the Internal Hellenides, Greece. *Tectonophysics* **2009**, *473*, 20–35. [[CrossRef](#)]
37. Himmerkus, F.; Reischmann, T.; Kostopoulos, D. Triassic rift-related meta-granites in the Internal Hellenides, Greece. *Geol. Mag.* **2009**, *146*, 252–265. [[CrossRef](#)]
38. Schmid, S.M.; Fügenschuh, B.; Kounov, A.; Matenco, L.; Nievergelt, P.; Oberhänsli, R.; Pleuger, J.; Schefer, S.; Schuster, R.; Tomljenović, B.; et al. Tectonic units of the Alpine collision zone between Eastern Alps and western Turkey. *Gondwana Res.* **2020**, *78*, 308–374. [[CrossRef](#)]
39. Mposkos, E.; Krohe, A.; Baziotis, I. Deep tectonics in the Eastern Hellenides uncovered: The record of Variscan continental amalgamation, Permo-Triassic rifting, and Early Alpine collision in Pre-Variscan continental crust in the W-Rhodope (Vertiscos-Ograzden Complex, NGreece). *Tectonics* **2021**, *40*, e2019TC005557. [[CrossRef](#)]
40. Kiliyas, A.; Falalakis, G.; Mountrakis, D. Cretaceous-Tertiary structures and kinematics of the Serbomacedonian metamorphic rocks and their relation to the exhumation of the Hellenic hinterland (Macedonia, Greece). *Int. J. Earth Sci.* **1999**, *88*, 513–531. [[CrossRef](#)]
41. Melidonis, N.G. Geology and mineralization of Pontokerasia (Kilkis area). *Ann. Geol. Pays Hell.* **1972**, *24*, 323–393. (In Greek)
42. Melidonis, N.G. *The Strymoniko-Metamorphosis Arc of Neo-Volcanic Rocks (Central Macedonia)*; Hellenic Survey of Geology and Mineral Exploration (HSGME): Athens, Greece, 1972; p. 51, (In Greek with German abstract).
43. Kockel, F.; Mollat, H.; Antoniadis, P.; Ioannidis, K. *Geological Map of Greece: Sochos Map Sheet, 1:50.000*; IGME: Athens, Greece, 1979.
44. Mercier, J. Mouvements orogéniques et magmatisme d'âge Jurassique Supérieur-Eocérocé dans les Zones Internes des Hellénides (Macédoine, Grèce). *Rev. Géogr. Phys.* **1966**, *8*, 265–278.
45. Michailidis, K.; Kassoli-Fournaraki, A. Tourmaline concentrations in migmatitic metasedimentary rocks of the Riziana and Kolchiko areas in Macedonia, Northern Greece. *Eur. J. Miner.* **1994**, *6*, 557–570. [[CrossRef](#)]
46. Christofides, G.; Koronaios, A.; Liati, A.; Kral, J. The A-type Kerkini granitic complex in north Greece: Geochronology and geodynamic implications. *Bull. Geol. Soc. Greece* **2007**, *40*, 700–711. [[CrossRef](#)]
47. Christofides, G.; Koroneos, A.; Pe-Piper, G.; Katirtzoglou, K.; Chatzikirkou, A. Pre-Tertiary A-type magmatism in the Serbomacedonian massif (N.Greece): Kerkini granitic complex. *Bull. Geol. Soc. Greece* **1999**, *33*, 131–148.
48. Panagos, A.G.; Pe, G.G.; Varnavas, S.P. The volcanic rocks of Strymonikon-Metamorphosis, Central Macedonia, Greece. *Chem. Erde* **1978**, *37*, 50–61.
49. Bakker, R.J. Package FLUIDS. Part 4: Thermodynamic modelling and purely empirical equations for H<sub>2</sub>O-NaCl-KCl solutions. *Mineral. Petrol.* **2012**, *105*, 1–29. [[CrossRef](#)]
50. Driesner, T.; Heinrich, C.A. The system H<sub>2</sub>O-NaCl. Part I: Correlations for molar volume, enthalpy, and isobaric heat capacity from 0 to 1000 degrees C, 1 to 5000 bar, and 0 to 1 X-NaCl. *Geochim. Cosmochim. Acta* **2007**, *71*, 4880–4901. [[CrossRef](#)]
51. Driesner, T. The system H<sub>2</sub>O-NaCl. Part II: Correlations for molar volume, enthalpy, and isobaric heat capacity from 0 to 1000 °C, 1 to 5000 bar, and 0 to 1 XNaCl. *Geochim. Cosmochim. Acta* **2007**, *71*, 4902–4919. [[CrossRef](#)]
52. McDonough, W.F.; Sun, S.-S. Composition of the Earth. *Chem. Geol.* **1995**, *120*, 223–253. [[CrossRef](#)]
53. Rudnick, R.L.; Gao, S. Composition of the continental crust. In *The Crust*, 1st ed.; Rudnick, R.L., Holland, H.D., Turekian, K.K., Eds.; Elsevier: Amsterdam, The Netherlands, 2005; pp. 1–64.
54. Monecke, T.; Monecke, J.; Reynolds, T.J.; Tsuruoka, S.; Bennett, M.M.; Skewes, W.B.; Palin, R.M. Quartz solubility in the H<sub>2</sub>O-NaCl System: A framework for understanding vein formation in porphyry copper deposits. *Econ. Geol.* **2018**, *113*, 1007–1046. [[CrossRef](#)]
55. Roedder, E. Fluid inclusions. *Rev. Miner.* **1984**, *12*, 644.
56. Goldstein, R.H.; Reynolds, T.J. *Systematics of Fluid Inclusions in Diagenetic Minerals*; Society for Sedimentary Geology: Broken Arrow, OK, USA, 1994; p. 199.
57. Bodnar, R.J. Introduction to fluid inclusions. In *Fluid Inclusions: Analysis and Interpretation*; Samson, I.M., Anderson, A.J., Marshall, D.D., Eds.; Society for Sedimentary Geology: Broken Arrow, OK, USA, 2003; Volume 32, pp. 1–8.
58. Potter, R.W.; Clynne, M.A.; Brown, D.L. Freezing point depression of aqueous sodium chloride solutions. *Econ. Geol.* **1978**, *73*, 284–285. [[CrossRef](#)]
59. Shepherd, T.; Rankin, A.; Alderton, D. *A Practical Guide to Fluid Inclusion Studies*, 1st ed.; Blackie and Son: Glasgow, UK, 1985; p. 239.
60. Mavrogonatos, C.; Voudouris, P.; Berndt, J.; Klemme, S.; Zaccarini, F.; Spry, P.G.; Melfos, V.; Tarantola, A.; Keith, M.; Klemm, R.; et al. Trace elements in magnetite from the Pagoni Rachi porphyry prospect, NE Greece: Implications for ore genesis and exploration. *Minerals* **2019**, *9*, 725. [[CrossRef](#)]

61. Mavrogonatos, C.; Voudouris, P.; Zaccarini, F.; Klemme, S.; Berndt, J.; Tarantola, A.; Melfos, V.; Spry, P.G. Multi-stage introduction of precious and critical metals in pyrite: A case study from the Konos Hill and Pagoni Rachi porphyry/epithermal prospects, NE Greece. *Minerals* **2020**, *10*, 784. [[CrossRef](#)]
62. Voudouris, P.; Repstock, A.; Spry, P.G.; Frenzel, M.; Mavrogonatos, C.; Keith, M.; Tarantola, A.; Melfos, V.; Tombros, S.; Zhai, D.; et al. Physicochemical constraints on indium-, tin-, germanium-, gallium-, gold-, and tellurium-bearing mineralizations in the Pefka and St Philippos polymetallic vein-and breccia-type deposits, Greece. *Ore Geol. Rev.* **2022**, *140*, 104348. [[CrossRef](#)]
63. Peristeridou, E.; Melfos, V.; Papadopoulou, L.; Kantiranis, N.; Voudouris, P. Mineralogy and Mineral Chemistry of the REE-Rich Black Sands in Beaches of the Kavala District, Northern Greece. *Geosciences* **2022**, *12*, 277. [[CrossRef](#)]
64. Voudouris, P.; Spry, P.G.; Melfos, V.; Alfieris, D. Tellurides and bismuth sulfosalts in gold occurrences of Greece: Mineralogical and genetic considerations. In *Gold Deposits in Finland*; Kojonen, K.K., Cook, N.J., Ojala, V.J., Eds.; Geological Survey of Finland: Espoo, Finland, 2007; Volume 53, pp. 85–94.
65. Stergiou, C.L. Critical and Rare Metals in Tertiary Magmatic-Mydrothermal Deposits at the Serbo-Macedonian Metallogenic Province in Greece (Vathi, Gerakario, Laodikino, Kolchiko, Aspra Chomata). Ph.D. Thesis, Faculty of Geology, Aristotle University of Thessaloniki, Thessaloniki, Greece, 2022.
66. Voudouris, P.; Spry, P.G.; Mavrogonatos, C.; Sakellaris, G.A.; Bristol, S.K.; Melfos, V.; Fornadel, A. Bismuthinite derivatives, lillianite homologues, and bismuth sulfotellurides as indicators of gold mineralization at the Stanos shear-zone related deposit, Chalkidiki, northern Greece. *Can. Mineral.* **2013**, *51*, 119–142. [[CrossRef](#)]
67. Bristol, S.K.; Spry, P.G.; Voudouris, P.C.; Melfos, V.; Mathur, R.D.; Fornadel, A.P.; Sakellaris, G.A. Geochemical and geochronological constraints on the formation of shear-zone hosted Cu–Au–Bi–Te mineralization in the Stanos area, Chalkidiki, northern Greece. *Ore Geol. Rev.* **2015**, *66*, 266–282. [[CrossRef](#)]
68. Stergiou, C.L.; Melfos, V.; Voudouris, P.; Papadopoulou, L.; Spry, P.G. Geology, mineralogy, and geochemistry of the intrusion-related polymetallic quartz veins at Laodikino, Serbo-Macedonian Massif, N. Greece. In Proceedings of the Abstract volume of the SEG100: Celebrating a Century of Discovery, Whistler, Canada, 14–17 September 2021.
69. Vavelidis, M.; Kiliyas, A.; Melfos, V.; Schmidt-Mumm, A. New investigations in the Au–Ag-bearing Cu mineralization and its structural control in the Koronouda area, central Macedonia, Northern Greece. In *Terranes of Serbia: The Formation of the Geologic Framework of Serbia and the Adjacent Regions: Dedicated to Academic Stevan Karamata*; Knežević, V., Krstić, B., Eds.; Faculty of Mining and Geology, University of Belgrade: Belgrade, Serbia; Committee for Geodynamics of the Serbian Academy of Sciences and Arts, Belgrade: Belgrade, Serbia, 1996; pp. 317–322.
70. Vavelidis, M.; Melfos, V.; Kiliyas, A. The gold-bearing quartz veins in the metamorphic rocks at the Drakontio area, central Macedonia, northern Greece. In *Mineral Deposits: Processes to Processing*; Stanley, C.J., Ed.; AA Balkema: Rotterdam, The Netherlands, 1999; pp. 209–212.
71. Mposkos, E. A new occurrence of argentian pentlandite from the Koronouda ore mineralization, Macedonia, Greece. *Neues Jahrb. Mineral.* **1983**, *5*, 193–200.
72. Melfos, V.; Vavelidis, M.; Arikas, K. A new occurrence of argentopentlandite and gold from the Au–Ag-rich copper mineralisation in the Paliomylos area, Serbomacedonian Massif, Central Macedonia, Greece. *Bull. Geol. Soc. Greece* **2001**, *34*, 1065–1072. [[CrossRef](#)]
73. Demir, Y.; Uysal, İ.; Kandemir, R.; Jauss, A. Geochemistry, fluid inclusion and stable isotope constraints (C and O) of the Sivrikaya Fe-skarn mineralization (Rize, NE Turkey). *Ore Geol. Rev.* **2017**, *91*, 153–172. [[CrossRef](#)]
74. Demir, Y.; Dişli, A. Fluid inclusion and stable isotope constraints (C, O, H) on the Dağbaşı Fe–Cu–Zn skarn mineralization (Trabzon, NE Turkey). *Ore Geol. Rev.* **2020**, *116*, 103235. [[CrossRef](#)]
75. Hedenquist, J.W.; Arribas, A.R.; Gonzalez-Unien, E. Exploration for epithermal gold deposits. In *Reviews in Economic Geology: Gold in 2000*; Hagemann, S.G., Brown, P.E., Eds.; Society of Economic Geologists: Littleton, CO, USA, 2000; pp. 245–277.
76. Brugger, J.; Liu, W.; Etschmann, B.; Mei, Y.; Sherman, D.M.; Testemale, D. A review of the coordination chemistry of hydrothermal systems, or do coordination changes make ore deposits? *Chem. Geol.* **2016**, *447*, 219–253. [[CrossRef](#)]
77. Collins, E.M.; Kesler, S.E. High temperature telescoped tungsten-antimony mineralization, Guatemala. *Miner. Depos.* **1969**, *4*, 65–71. [[CrossRef](#)]
78. Bailly, L.; Grancea, L.; Kouzmanov, K. Infrared microthermometry and chemistry of wolframite from the Baia Sprie epithermal deposit, Romania. *Econ. Geol.* **2002**, *97*, 415–423. [[CrossRef](#)]

**Disclaimer/Publisher’s Note:** The statements, opinions and data contained in all publications are solely those of the individual author(s) and contributor(s) and not of MDPI and/or the editor(s). MDPI and/or the editor(s) disclaim responsibility for any injury to people or property resulting from any ideas, methods, instructions or products referred to in the content.